

See discussions, stats, and author profiles for this publication at: <https://www.researchgate.net/publication/227024007>

# Investigation of high frequency noise generation in the near-nozzle region of a jet using large eddy simulation

ARTICLE *in* THEORETICAL AND COMPUTATIONAL FLUID DYNAMICS · JULY 2007

Impact Factor: 1.8 · DOI: 10.1007/s00162-007-0048-z

---

CITATIONS

32

---

READS

35

2 AUTHORS, INCLUDING:



Mohammed Yousuff Hussaini

Florida State University

370 PUBLICATIONS 10,358 CITATIONS

SEE PROFILE

Ali Uzun · M. Yousuff Hussaini

## Investigation of high frequency noise generation in the near-nozzle region of a jet using large eddy simulation

Received: 26 June 2006 / Accepted: 13 March 2007 / Published online: 8 May 2007  
© Springer-Verlag 2007

**Abstract** This paper reports on the simulation of the near-nozzle region of an isothermal Mach 0.6 jet at a Reynolds number of 100,000 exhausting from a round nozzle geometry. The flow inside the nozzle and the free jet outside the nozzle are computed simultaneously by a high-order accurate, multi-block, large eddy simulation (LES) code with overset grid capability. The total number of grid points at which the governing equations are solved is about 50 million. The main emphasis of the simulation is to capture the high frequency noise generation that takes place in the shear layers of the jet within the first few diameters downstream of the nozzle exit. Although we have attempted to generate fully turbulent boundary layers inside the nozzle by means of a special turbulent inflow generation procedure, an analysis of the simulation results supports the fact that the state of the nozzle exit boundary layer should be characterized as transitional rather than fully turbulent. This is believed to be most likely due to imperfections in the inflow generation method. Details of the computational methodology are presented together with an analysis of the simulation results. A comparison of the far field noise spectrum in the sideline direction with experimental data at similar flow conditions is also carried out. Additional noise generation due to vortex pairing in the region immediately downstream of the nozzle exit is also observed. In a second simulation, the effect of the nozzle exit boundary layer thickness on the vortex pairing Strouhal frequency (based on nozzle diameter) and its harmonics is demonstrated. The limitations and deficiencies of the present study are identified and discussed. We hope that the lessons learned in this study will help guide future research activities towards resolving the pending issues identified in this work.

**Keywords** Jet noise · Shear layers · Large eddy simulation · Computational aeroacoustics

**PACS** 47.27.nb · 47.27.ep · 47.27.Sd · 47.27.W · 47.27.N-

---

Communicated by T. Colonius.

---

Presented as AIAA Paper 2006-2499 at 12th AIAA/CEAS Aeroacoustics Conference, 8–10 May 2006, Cambridge, MA, USA.

---

A. Uzun · M. Y. Hussaini (✉)  
School of Computational Science, Florida State University,  
Tallahassee, FL 32306-4120, USA  
E-mail: myh@scs.fsu.edu

A. Uzun  
E-mail: uzun@scs.fsu.edu

## List of symbols

$c$	sound speed
$D$	spatial derivative
$D_j$	jet nozzle diameter
$e_t$	total energy, $\rho(u^2 + v^2 + w^2)/2 + p/(\gamma - 1)$
$f$	arbitrary variable; frequency
<b>F, G, H</b>	inviscid flux vectors in Navier–Stokes equations
<b>F<sub>v</sub>, G<sub>v</sub>, H<sub>v</sub></b>	viscous flux vectors in Navier–Stokes equations
$i, j, k$	grid point indices
$J$	metric Jacobian
$L$	integral length scale
$N$	number of grid points along given spatial direction
$p$	static pressure
$Q$	vector of conservative flow variables
<b>Q</b>	$Q/J$
$Re_D$	jet nozzle Reynolds number, $\rho_j U_j D_j / \mu_j$
$Re_\theta$	momentum thickness Reynolds number, $\rho_j U_j \delta_\theta / \mu_j$
$\mathcal{R}_{rr}$	two-point velocity correlation in radial direction
$\mathcal{R}_{\theta\theta}$	two-point velocity correlation in azimuthal direction
$\mathcal{R}_{xx}$	two-point velocity correlation in streamwise direction
$Sr_D$	Strouhal number, $f D_j / U_j$
$t$	time
$U$	mean streamwise velocity
$u_\tau$	friction velocity, $\sqrt{\tau_{\text{wall}} / \rho_{\text{wall}}}$
$u, v, w$	Cartesian velocity components in $x$ , $y$ , and $z$ directions
$x, y, z$	Cartesian coordinates
$\alpha_f$	filtering parameter
$\delta_{\text{exit}}$	boundary layer thickness at nozzle exit
$\delta_{\text{inlet}}$	boundary layer thickness at nozzle inlet
$\delta_{\text{recycle}}$	boundary layer thickness at recycle station
$\delta_\theta$	momentum thickness of boundary layer
$\Delta_r$	wall normal or radial grid spacing
$\Delta_\theta$	azimuthal grid spacing
$\Delta_x$	streamwise grid spacing
$\Delta t$	time increment
$\Delta\xi$	uniform grid spacing along $\xi$ direction in the computational domain
$\epsilon_I$	artificial dissipation parameter in implicit time stepping
$\gamma$	ratio of specific heats of air, 1.4
$\mu$	molecular viscosity
$\nu$	kinematic viscosity ( $\mu/\rho$ )
$\rho$	fluid density
$\sigma_{ijk}$	spectral radius of inviscid flux Jacobian at grid point $(i, j, k)$
$\tau$	wall shear stress; time scale
$\xi, \eta, \zeta$	generalized curvilinear coordinates
$\langle \rangle$	time averaging operator
Subscripts	
$i$	value at grid point $i$
$\infty$	ambient value
$j$	value at nozzle exit centerline
$r$	radial direction
rms	root mean squared
$x$	streamwise direction
$\theta$	azimuthal direction; value based on momentum thickness
wall	value on nozzle wall

## Superscripts

$B$	backward operator in prefactored optimized compact scheme
$F$	forward operator in prefactored optimized compact scheme
$n$	time level
$\overline{(\quad)}$	spatially filtered quantity
$p$	sub-iteration level
$+$	value given in wall units
$'$	perturbation from mean value
$\tilde{(\quad)}$	Favre-filtered quantity

## 1 Introduction

Jet noise reduction is one of the major issues concerning jet engine manufacturers. Strict noise regulations around major airports have made jet noise a crucial problem in present day aeroacoustics research, as it is the jet engine exhaust that is responsible for most of the noise generation during aircraft takeoff. The importance of the problem has motivated numerous experimental and computational studies. Most of the recent computational studies in this area have used large eddy simulation (LES) techniques, as such simulation techniques have shown some promise in successful jet noise prediction. A recent review of the use of LES in jet noise prediction is provided by Bodony and Lele [12]. Although LES is becoming a popular choice in computational jet noise research, the jet nozzle geometry has usually been excluded from the computations in order to reduce computing resource requirements and make the simulations more affordable. In the majority of jet simulations done to date, the usual practice has been to start the computational domain slightly downstream of the nozzle exit and feed laminar jet shear layers into the domain. To force transition to turbulence, some sort of artificial excitation, such as randomized velocity perturbations, have been injected into the jet shear layers. On the other hand, experiments are usually performed at high enough Reynolds numbers so that the jet shear layers at the nozzle exit are fully turbulent. The mismatch of the inflow conditions in the numerical simulations with those in the actual experiments is believed to be one of the reasons for the discrepancies observed when experimental and computational noise spectra are compared. Moreover, it has been observed experimentally [32] that high frequency sources are located within a few diameters downstream of the jet nozzle exit and a significant portion of the noise spectrum in the sideline direction, that is, at around 90 degrees perpendicular to the jet axis, originates from this near field region of the jet. Hence, the high frequency noise generated in the near-nozzle jet shear layer within a few diameters downstream of the nozzle exit is missing in the simulations that exclude the nozzle and start out with laminar shear layers instead. The low frequency noise sources, on the other hand, are located near the end of the jet potential core and further downstream, and the low frequency noise radiation in the downstream direction has been captured reasonably well by some LES calculations that have not included the nozzle geometry.

It now appears that more realistic jet inflow conditions are needed in order to better match experimental acoustic data, especially in the sideline direction. One way to accomplish this objective is to include the nozzle as part of the computation. This, of course, increases the overall computational cost. However, with significant advances taking place in computing technology, perhaps the time has already come for such simulations. The recent studies of Lupoglazoff et al. [29], Biancherin et al. [10], DeBonis and Scott [17], DeBonis [16], Andersson et al. [3–5], Paliath and Morris [33,34], Wu et al. [55], Barré et al. [7] and Viswanathan et al. [54] are some of the first computations that have included the nozzle geometry as part of the simulation and have produced some promising results. Yet, the grid resolution in the near-nozzle region in these studies is still not sufficiently small to capture the very high frequency noise generation in the jet shear layers. As mentioned earlier, the noise spectra in the sideline direction is dominated by high frequency noise that is generated in the jet shear layers within a few diameters of the nozzle exit. When adjusted from model scale to jet engine scale, the high frequencies translate into the frequencies that contribute the most to human hearing and annoyance [32]. A numerical computation that includes the nozzle geometry should attempt to capture the flow physics in the near-nozzle shear layers as accurately as possible in order to successfully predict the noise radiation in the sideline direction. This, of course, means that a good amount of grid resolution is required in the near-nozzle shear layers. Moreover, it is the turbulent boundary layers of the nozzle flow that feed fine scale turbulence into the shear layers of the jet. The numerical computation that attempts to capture the high frequency noise generation in the near-nozzle region should resolve the turbulent boundary layers within the nozzle as well. It is also worth mentioning at this point that although detached eddy simulation (DES) is a possible option for

reducing the computational cost of jet flow computations including nozzle geometries, it is still not clear how successful DES will be if the aim is to successfully predict the high frequency noise. The DES approach uses Reynolds-averaged Navier Stokes (RANS) methods to model the turbulence in the nozzle boundary layers, and LES for the free jet flow outside the nozzle. Unfortunately, the turbulence in the nozzle boundary layers plays a crucial role in the near-nozzle high frequency noise generation, and using RANS in such an important region for the problem of interest may not yield satisfactory predictions.

It is, therefore, the purpose of the present study to conduct an LES of both the flow inside a round nozzle and the jet flow within a few diameters downstream of the nozzle exit with the best grid resolution that current computing resources allow. This, of course, means that the jet Reynolds number will have to be moderate. As will be evident later, even for the moderate Reynolds number considered in this study, available computing resources unfortunately will not allow the extension of the computational domain all the way to the fully turbulent region of the jet in the far downstream region. However, the fully turbulent region downstream of jet potential core end mainly generates low frequency noise. The experimental study of Narayanan et al. [32] reports that the main contribution to the noise intensity for high frequencies in the range  $2 \leq Sr_D \leq 10$  occurs in the region  $0 \leq x/D_j \leq 3$ , where the non-dimensional frequency (Strouhal number) is defined as  $Sr_D = f D_j / U_j$ ,  $x$  is the streamwise distance downstream of the nozzle exit,  $f$  is the dimensional frequency,  $D_j$  is the jet nozzle diameter and  $U_j$  is the jet centerline velocity at the nozzle exit.

In the present study, we perform reasonably well-resolved numerical computations of both the nozzle flow and the free jet flow in the near-nozzle region and explore how well the near-nozzle high frequency noise generation is captured. An inflow generation technique similar to that of Lund et al. [28] is applied in an attempt to generate fully turbulent boundary layers inside the nozzle. However, as will be seen later, an analysis of the simulation results provides evidence that the state of the nozzle exit boundary layer in the present simulations should be characterized as transitional rather than fully turbulent. The calculations are performed by a high-order accurate, multi-block LES solver with overset grid capability whose details will be presented in the next section.

## 2 Computational methodology

In this study, the Favre-filtered, unsteady, compressible, non-dimensional Navier–Stokes equations formulated in curvilinear coordinates, which are expressed in the following conservative form, are solved:

$$\frac{\partial \mathbf{Q}}{\partial t} = - \left[ \frac{\partial}{\partial \xi} \left( \frac{\mathbf{F} - \mathbf{F}_v}{J} \right) + \frac{\partial}{\partial \eta} \left( \frac{\mathbf{G} - \mathbf{G}_v}{J} \right) + \frac{\partial}{\partial \zeta} \left( \frac{\mathbf{H} - \mathbf{H}_v}{J} \right) \right] \quad (1)$$

Here,  $t$  is the time,  $\xi$ ,  $\eta$ , and  $\zeta$  are the generalized curvilinear coordinates of the computational space, and  $J$  is the Jacobian of the coordinate transformation from the physical domain to the computational domain.  $\mathbf{Q} = \mathbf{Q}/J$  where  $\mathbf{Q} = [\bar{\rho}, \bar{\rho}\tilde{u}, \bar{\rho}\tilde{v}, \bar{\rho}\tilde{w}, \bar{e}_t]^T$  is the vector of conservative flow variables,  $\mathbf{F}$ ,  $\mathbf{G}$ , and  $\mathbf{H}$  are the inviscid flux vectors, and  $\mathbf{F}_v$ ,  $\mathbf{G}_v$ , and  $\mathbf{H}_v$  are the viscous flux vectors. The details of the governing equations can be found in Rizzetta et al. [38] or in Uzun [45].

A single-block LES code that was previously developed by the first author during his doctoral dissertation research [45,46,48] has been extended to a multi-block version. Gaitonde and Visbal [22] as well as Visbal and Gaitonde [49] have investigated multi-block implementation strategies in which high-order compact schemes are simultaneously employed in every sub-domain and grid point overlaps are used to exchange data between adjacent sub-domains during the course of the computations. The attractiveness of this technique is that it allows high-order accurate simulations to be performed in complex domains using multi-block structured grids. A multi-block implementation strategy similar to that of Gaitonde and Visbal [22] is incorporated in the multi-block version of the LES code with a seven-point grid overlap between neighboring blocks. The standard message passing interface library routines have been used in the code parallelization.

We now consider an individual block of the multi-block grid. The non-uniformly spaced curvilinear grid in physical space is transformed to a uniform grid in computational space and the discretized governing equations are solved on the uniform grid. High-order compact finite difference schemes are used to compute the spatial derivatives in the governing equations. The fourth-order optimized prefactored compact schemes recently developed by Ashcroft and Zhang [6] offer improved dispersion characteristics compared to the standard sixth-order and eighth-order compact schemes [27]. The prefactorization strategy splits the central implicit schemes into forward and backward biased operators. The prefactored optimized schemes require the solution of two

independent bi-diagonal matrices. The spatial derivative at a given grid point,  $i$ , is given by

$$D_i = \frac{1}{2} (D_i^F + D_i^B) \quad (2)$$

where  $D_i^F$  and  $D_i^B$  represent the forward and backward operators, respectively. The prefactored compact scheme we use is a fourth-order scheme with a five-point stencil. Hence, the forward and backward operators are given as follows:

$$\frac{1}{2} D_i^F = \frac{1}{2\beta\Delta\xi} [b(f_{i+1} - f_i) + d(f_{i-1} - f_i) + e(f_{i-2} - f_i)] - \frac{\alpha}{2\beta} D_{i+1}^F \quad (3)$$

$$\frac{1}{2} D_i^B = \frac{1}{2\beta\Delta\xi} [b(f_i - f_{i-1}) + d(f_i - f_{i+1}) + e(f_i - f_{i+2})] - \frac{\alpha}{2\beta} D_{i-1}^B, \quad (4)$$

where the coefficients  $\alpha, \beta, b, d, e$  are given by Ashcroft and Zhang [6],  $f_i$  denotes the value of  $f$  (the quantity whose spatial derivative is being computed) at grid point  $i$ , and  $\Delta\xi$  is the uniform grid spacing along a given spatial direction in the computational space. The above scheme is applicable to grid points  $i = 3$  through  $i = N - 2$ , where  $N$  is the number of grid points along the spatial direction. Additional boundary stencils are required at grid points  $i = 1, 2$  and  $i = N - 1, N$ . The third-order boundary stencils we use are given by Ashcroft and Zhang [6]. At grid points  $i = 2$  and  $i = N - 1$ , the following explicit backward and forward stencils are used:

$$D_2^B = \frac{1}{\Delta\xi} \sum_{i=1}^4 s_i f_i, \quad D_{N-1}^B = \frac{1}{\Delta\xi} \sum_{i=N-3}^N e_i f_i \quad (5)$$

$$D_2^F = \frac{1}{\Delta\xi} \sum_{i=1}^4 -e_{N+1-i} f_i, \quad D_{N-1}^F = \frac{1}{\Delta\xi} \sum_{i=N-3}^N -s_{N+1-i} f_i \quad (6)$$

The coefficients  $s_i$  ( $i = 1, \dots, 4$ ) and  $e_i$  ( $i = N - 3, \dots, N$ ) are given by Ashcroft and Zhang [6]. At grid points  $i = 1$  and  $i = N$ , the following one-sided explicit schemes are employed to compute the spatial derivative:

$$D_1 = \frac{1}{\Delta\xi} \sum_{i=1}^4 c_i f_i, \quad D_N = \frac{1}{\Delta\xi} \sum_{i=N-3}^N -c_{N+1-i} f_i \quad (7)$$

where  $c_1 = -33/18$ ,  $c_2 = 3$ ,  $c_3 = -3/2$  and  $c_4 = 1/3$ .

The viscous stress terms appearing in the governing equations are obtained using the first-derivatives of the velocity components. The spatial derivatives of the inviscid and viscous flux vectors are computed using the prefactored optimized compact scheme. As a consequence of such an implementation, the second-derivatives in the viscous fluxes are essentially evaluated by the application of the first-derivative operator twice. Although this approach is not as accurate as when a compact scheme is used to directly compute the second-derivatives in the viscous terms, it is much cheaper to implement in curvilinear coordinates. We should also note here that for computational efficiency, the terms in the inviscid and viscous fluxes can be added together and then the total flux can be differentiated. However, the characteristic-type boundary conditions implemented on solid walls (to be discussed shortly) require the separation of inviscid and viscous fluxes; hence, we compute the inviscid and viscous flux derivatives separately in this work.

The LES code also employs the following sixth-order tri-diagonal spatial filter used by Visbal and Gaitonde [49]:

$$\alpha_f \bar{f}_{i-1} + \bar{f}_i + \alpha_f \bar{f}_{i+1} = \sum_{n=0}^3 \frac{a_n}{2} (f_{i+n} + f_{i-n}) \quad (8)$$

where  $\bar{f}_i$  denotes the filtered value of quantity  $f$  at grid point  $i$ , and

$$a_0 = \frac{11}{16} + \frac{5\alpha_f}{8}, \quad a_1 = \frac{15}{32} + \frac{17\alpha_f}{16}, \quad a_2 = \frac{-3}{16} + \frac{3\alpha_f}{8}, \quad a_3 = \frac{1}{32} - \frac{\alpha_f}{16} \quad (9)$$

The parameter  $\alpha_f$  must satisfy the inequality  $-0.5 < \alpha_f < 0.5$ . A less dissipative filter is obtained with higher values of  $\alpha_f$  within the given range. With  $\alpha_f = 0.5$ , there is no filtering effect since Eq. 8 reduces to an identity.

Since this filter has a seven-point right-hand side stencil, it obviously cannot be used at near-boundary points. Instead, the following sixth-order equation with a one-sided right-hand side stencil is used at grid points near the left boundary point  $i = 1$ :

$$\alpha_f \bar{f}_{i-1} + \bar{f}_i + \alpha_f \bar{f}_{i+1} = \sum_{n=1}^7 a_{n,i} f_n, \quad i = 2, 3 \quad (10)$$

where the coefficients,  $a_{n,i}$  are given by Visbal and Gaitonde [49]. For the points near the right boundary point  $i = N$ , we apply a similar formulation [49]. The boundary points,  $i = 1$  and  $i = N$  are left unfiltered.

The filtering process eliminates the spurious high frequency numerical oscillations and ensures numerical stability. Numerical tests show that values of the filtering parameter,  $\alpha_f$ , between 0.45 and 0.49 effectively eliminate the spurious oscillations while providing very little dissipation and hence leave the well-resolved scales mostly unaffected. A value of  $\alpha_f = 0.47$ , which is in the middle of this range, has been used in the present simulation.

Time advancement can be performed by means of either the standard fourth-order, four-stage explicit Runge–Kutta scheme or a second-order Beam–Warming type implicit time integration scheme [8,20]. The iterative form of the approximately factored finite-difference algorithm of Beam and Warming that is second-order accurate in time can be represented as

$$\begin{aligned} & \left[ \mathbf{I} + \frac{2\Delta t}{3} \frac{\partial}{\partial \xi} \left( \frac{\partial \mathbf{F}}{\partial \mathbf{Q}} - \frac{\partial \mathbf{F}_v}{\partial \mathbf{Q}} \right) \right]^p \times \left[ \mathbf{I} + \frac{2\Delta t}{3} \frac{\partial}{\partial \eta} \left( \frac{\partial \mathbf{G}}{\partial \mathbf{Q}} - \frac{\partial \mathbf{G}_v}{\partial \mathbf{Q}} \right) \right]^p \times \left[ \mathbf{I} + \frac{2\Delta t}{3} \frac{\partial}{\partial \zeta} \left( \frac{\partial \mathbf{H}}{\partial \mathbf{Q}} - \frac{\partial \mathbf{H}_v}{\partial \mathbf{Q}} \right) \right]^p \Delta \mathbf{Q}^p \\ & = - \left[ \mathbf{Q}^p - \frac{4}{3} \mathbf{Q}^n + \frac{1}{3} \mathbf{Q}^{n-1} \right] - \frac{2\Delta t}{3} \left[ \frac{\partial}{\partial \xi} (\mathbf{F} - \mathbf{F}_v) + \frac{\partial}{\partial \eta} (\mathbf{G} - \mathbf{G}_v) + \frac{\partial}{\partial \zeta} (\mathbf{H} - \mathbf{H}_v) \right]^p. \end{aligned} \quad (11)$$

The superscript  $p$  denotes the sub-iteration level,  $\mathbf{I}$  represents the identity matrix,  $\Delta t$  is the time step and  $\Delta \mathbf{Q}^p = \mathbf{Q}^{p+1} - \mathbf{Q}^p$ . For  $p = 1$ ,  $\mathbf{Q}^p = \mathbf{Q}^n$ , where  $n$  represents the current time level, and  $n - 1$  represents the previous time level.  $\mathbf{Q}^{p+1}$  is the  $p + 1$  approximation to the solution at the  $n + 1$  time level,  $\mathbf{Q}^{n+1}$ . After several sub-iterations at each time step,  $\Delta \mathbf{Q}^p$  converges toward zero. A second-order accurate, three-point scheme is used to calculate the time derivative on the right-hand side of Eq. 11. It is well known that although the Beam–Warming scheme is unconditionally stable in two dimensions, it becomes unstable in three dimensions. To conditionally stabilize the scheme for the 3-D computations, we make use of artificial dissipation [36] in the implicit side of Eq. 11. For example, while applying the equation along the  $\xi$  direction, the artificial dissipation operator is appended to the implicit operator as follows

$$\left[ \mathbf{I} + \frac{2\Delta t}{3} \frac{\partial}{\partial \xi} \left( \frac{\partial \mathbf{F}}{\partial \mathbf{Q}} - \frac{\partial \mathbf{F}_v}{\partial \mathbf{Q}} \right) - \epsilon_I \nabla_\xi (\sigma_{i+1,j,k} J_{i+1,j,k}^{-1} + \sigma_{i,j,k} J_{i,j,k}^{-1}) \Delta_\xi J \right]^p, \quad (12)$$

where  $\nabla_\xi f_{i,j,k} = f_{i,j,k} - f_{i-1,j,k}$ ,  $\Delta_\xi f_{i,j,k} = f_{i+1,j,k} - f_{i,j,k}$ ,  $\sigma_{i,j,k}$  is the spectral radius of the inviscid flux Jacobian  $(\partial \mathbf{F} / \partial \mathbf{Q})$  at grid point  $(i, j, k)$ , and  $\epsilon_I$  controls the strength of the artificial dissipation.  $\epsilon_I = 0.5 \Delta t$  was found to provide adequate artificial dissipation to maintain stability. We should also note here that the somewhat cumbersome evaluation of the viscous flux Jacobians in generalized curvilinear coordinates is skipped in this work. Our experience shows that as several sub-iterations are applied per time step, neglecting the viscous flux Jacobians does not negatively impact the convergence of the scheme. The spatial derivatives operating on the fluxes on the right-hand side are computed using the prefactored optimized compact scheme described previously. On the other hand, the spatial derivatives operating on the flux Jacobians on the left-hand side are computed using the fourth-order compact scheme from Lele [27]. Use of compact schemes to attain high-order spatial accuracy for the implicit operators was originally proposed by Ekaterinaris [20]. The implicit time stepping algorithm we have implemented then becomes truly second-order accurate in time and fourth-order accurate in space. Application of compact schemes for the implicit operators results in a block tri-diagonal matrix system along each of the three computational directions, which are solved sequentially as described by Ekaterinaris [20]. This procedure basically replaces the three-dimensional problem by three one-dimensional problems at a given time level. Numerical experiments have shown that typically two or three sub-iterations per time step are sufficient to reduce the errors due to approximate factorization, linearization,



artificial dissipation and consequently drive  $\Delta \mathbf{Q}^p$  towards zero at each time step. The solution is filtered after every sub-iteration in order to ensure numerical stability.

A procedure similar to that of Lund et al. [28] is used in an attempt to generate fully turbulent boundary layers at the nozzle inlet. This is a method that was originally developed for generating three-dimensional, time-dependent turbulent inflow data for spatially developing zero-pressure gradient incompressible boundary layers. In this approach, instantaneous planes of velocity data are extracted at a specified location downstream of the inlet boundary. The velocity field is then rescaled according to boundary layer similarity laws and re-introduced at the inlet. The streamwise pressure gradient in a nozzle flow, although not strictly equal to zero, is only weakly favorable. Hence, we expect the method of Lund et al. [28] to work reasonably well for the turbulent inflow boundary layer generation in a round nozzle flow as well. Since implicit time stepping is used in the present simulation, the inflow conditions at the nozzle inlet are specified in terms of time derivatives. It should also be re-iterated that the method of Lund et al. [28] was originally developed for incompressible flows. However, the same method has been commonly used for recycling the velocity field in compressible flows as well (see, for example, the work of Sagaut et al. [39] for a review of the methods used in compressible flows.) Additionally, for compressible flows, a rescaling law for two thermodynamic variables is needed. See the work of Sagaut et al. [39] for the various rescaling methods of thermodynamic variables used in compressible flow applications. Following Sagaut et al. [39], we recycle temperature and pressure on the inflow boundary using the same recycling method they used, but we do the recycling only inside the boundary layer. Outside the boundary layer, temperature and pressure are set to constant values. The two regions are then smoothly blended. Admittedly, imposing a constant pressure and temperature outside the boundary layer makes the nozzle inflow boundary a reflecting type of boundary. In acoustics applications, one would ideally like to impose only the velocity fluctuations on the inflow boundary and compute pressure and density (or temperature) using some kind of non-reflecting boundary condition. Our experience shows that this is extremely difficult, if not impossible, to achieve in practice. We experimented with several non-reflecting type boundary conditions on the entire inflow boundary while imposing only the velocity fluctuations computed using the rescaling–recycling procedure. However, numerical instability was observed in all cases we tried. We believe the problem is due to the interaction of strong velocity fluctuations in the boundary layer with the existing non-reflecting boundary condition formulations. We also tried another approach in which the non-reflecting boundary condition was applied only outside the boundary layer while the pressure and temperature inside the boundary layer were obtained from the rescaling–recycling procedure. However, trying to blend the non-reflecting part of the inflow boundary with the boundary layer region was found to result in numerical instabilities as well. Given these difficulties, our only choice was to keep the pressure and temperature fixed outside the boundary layer on the nozzle inflow boundary, as mentioned earlier. Nevertheless, in the present application, noise is generated exterior to the nozzle, and propagates mostly in the lateral and downstream directions. Thus, we do not believe that there is significant acoustic wave reflection from the nozzle inflow boundary to have a strong impact on the results. A stable formulation of non-reflecting boundary conditions in combination with velocity perturbations computed using the inflow generation technique is highly desirable and can be an interesting topic for future research. As mentioned earlier, although we have attempted to generate fully turbulent boundary layers inside the nozzle, an analysis of the results later in this paper will provide evidence supporting the fact that the nozzle exit boundary layer is in a transitional rather than fully turbulent state. The fact that the boundary layer at the nozzle exit is not fully turbulent indicates problems with either the inflow generation method or the implicit LES (ILES) approach we are using (to be discussed shortly). However, as will be discussed soon, the ILES approach has been used successfully in wall-bounded problems by other researchers using numerical methods very similar to what we are using. Thus, we believe the inflow generation method is the primary suspect that is responsible for the lack of a fully turbulent boundary layer at the nozzle exit. Finally, we should mention that the rescaling and recycling of velocity, pressure and temperature could cause acoustic disturbances, as can the blending of the boundary layer with the core of the nozzle inlet where pressure and temperature are artificially held fixed. The procedure employed here could possibly result in acoustic resonance in the recycle region as well, which can have an effect on the development of downstream jet. These possibly problematic issues need to be carefully investigated to ensure the inflow generation procedure employed here does not have a strong negative impact on the development of the downstream jet. This is another area for future work.

Tam and Dong radiation boundary conditions modified by Dong [18] are applied on the boundaries to which only acoustic disturbances are reaching. In contrast to the original Tam and Dong radiation boundary conditions, the Dong-modified radiation boundary conditions do not require any knowledge of the local mean flow on the radiation boundaries. Outflow boundaries are handled by characteristic-type outflow boundary conditions [25]. We additionally attach a sponge zone downstream of the physical domain and apply grid stretching



in combination with artificial damping in this region in order to dissipate the turbulence in the flow field before it reaches the outflow boundary. This way, unwanted numerical reflections from the outflow boundary are suppressed. On solid walls, a generalized characteristic-type solid wall boundary condition [26] is applied. The wall temperature is computed using either isothermal or adiabatic boundary conditions. Application of the boundary conditions when explicit time stepping is used is straightforward. In this case, on the boundary points, the residual on the right-hand side of equation 1 is simply overwritten by the boundary conditions. In the case of implicit time stepping on the boundary points, the sum of the flux derivatives appearing on the right-hand side of Eq. 11 is replaced by the boundary conditions. Moreover, when solid wall boundaries are present, the block tri-diagonal system of equations must be modified such that all velocity components on viscous walls are enforced to be zero.

At every time step, the solution is advanced independently in each block. Information is exchanged among the blocks at the end of each stage of the Runge–Kutta time integration scheme or after every sub-iteration of the implicit time integration scheme, as well as after each application of the filter.

No explicit subgrid-scale (SGS) model is used in the present LES calculations. Instead, the spatial filter implemented in the LES is treated as an implicit SGS model. Thus, the approach we use here belongs to the implicit LES (ILES) class of methods. It is well understood in turbulent flows that the energy cascade is associated with a mean flux of energy that is directed from large scales towards small scales. The large scales contain the major part of the turbulent kinetic energy and they continuously feed the turbulent kinetic energy via the cascade to the smallest eddies, where it is dissipated. Since the grid resolution in an LES is too coarse to resolve all of the relevant length scales, the pile-up of energy at the high wavenumbers can be eliminated through the use of a spatial filter. Hence, the spatial filter can be thought of as an effective SGS model in an LES. In support of this observation, Visbal and Rizzetta [51] and Visbal et al. [50] have recently performed LES of turbulent channel flow and compressible isotropic turbulence decay without using any explicit subgrid-scale (SGS) model. In those simulations, they used high-order compact finite difference schemes and spatial filters similar to what are using. Spatial filtering was treated as an implicit SGS model in their calculations. They also showed that use of an SGS model in those simulations did not produce results superior to those obtained without employing an SGS model. While there is some concern about the use of ILES type methods in the near-wall region where viscosity plays a dominant role, we believe the near-wall boundary layer resolution in this study (to be discussed in the next section) is sufficient for the ILES approach to be accurate in this region. In fact, as will be seen, the boundary layer grid resolution used in this study is better than that used in the study done by Visbal and Rizzetta [51] on the comparison of the ILES approach with explicit SGS models in turbulent channel flow.

We have also implemented overset grid capability into our multi-block LES code. The overset grid approach (also known as Chimera; see, for example, Benek et al. [9]) provides added flexibility in meshing domains around complex geometries and is useful for avoiding grid point singularities. For example, when one uses a cylindrical grid to simulate a round jet, a polar singularity arises at the center of the cylindrical grid. Although there are several techniques to deal with the centerline singularity, such as those proposed by Mohseni and Colonius [31] and by Constantinescu and Lele [15], the present work takes a different approach. We use overset grids to avoid the centerline singularity, that is, we use a rectangular grid in the core region and surround it by an annular grid, as shown in Fig. 1. Since the points in the overlapping regions between these two grids are not coincident, interpolation is necessary to exchange information between these two grids. The grid arrangement shown in the figure also eliminates the extremely and unnecessarily small azimuthal grid spacings near the centerline, which are inevitable when the cylindrical grid extends all the way to the centerline.

It was previously shown by Sherer and Scott [41] that the use of second-order interpolation at overset grid boundaries results in a globally second-order accurate solution even when high-order compact differencing and filtering are used. Hence, we employ sixth-order accurate explicit Lagrangian interpolation in this work in conjunction with the high-order compact differencing and filtering schemes implemented in our code to ensure that a high-order accurate numerical solution is maintained throughout the entire computational domain. Sherer and Scott [41] demonstrate that the use of high-order, non-optimized explicit Lagrangian interpolation schemes in combination with high-order compact finite difference and filtering schemes produces acceptable results for several linear and non-linear benchmark problems, thus providing validation for their overall algorithm which is very similar to what are using. In our work, the sixth-order interpolation stencils are pre-computed by the OGEN program [23] which was developed at the Lawrence Livermore National Laboratory. An intermediate program reads in the output of OGEN and re-organizes the data for use with our LES code. The 3-D interpolation stencil consists of seven points along each of the three computational coordinate directions. The interpolation process takes place in the computational space. We should also mention here that OGEN

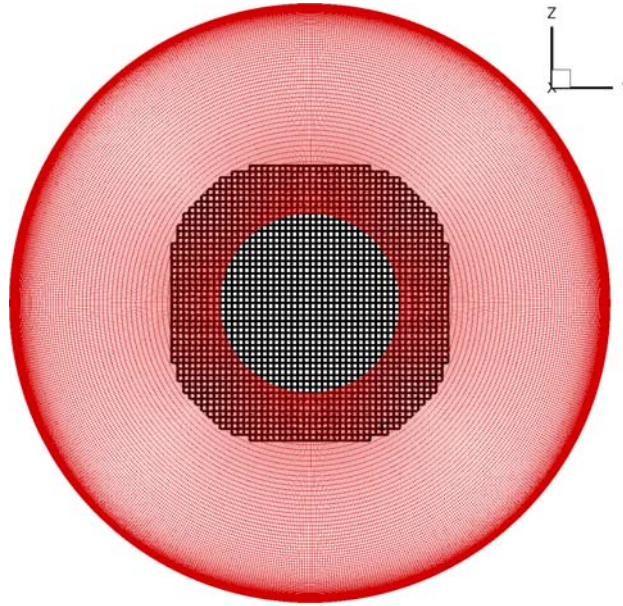


**Fig. 1** Jet core rectangular grid (shown in black) and the annular grid surrounding it

computes the location of the interpolation points within the computational space of a donor grid with only second-order accuracy. If sixth-order accuracy is desired in the interpolation process, then the location of the interpolation points within the computational space must be determined with sixth-order accuracy as well. For this purpose, a pre-processing program makes use of the interpolation stencils given by OGEN and computes the location of the interpolation points with sixth-order accuracy using a procedure described by Sherer and Scott [41].

The overset grid code used in the present study was originally developed for the simulation of wing tip vortices [47]. This code is intended to be a general purpose flow solver that is applicable to a wide variety of turbulence and aeroacoustics problems. Thus, the code was easily customized to the present simulation with minimal changes.

Far field noise computations are performed by coupling the time-accurate, unsteady near-field data provided by the LES with the Ffowcs Williams–Hawkings (FWH) method [30,48]. In our implementation, we apply the FWH method on the fly, that is, while the LES is running and computing unsteady data on the FWH control surface. The additional subroutine included in the LES code for the application the FWH method on the fly requires negligible computing cost as compared to the main LES.

### 3 Estimation of the grid resolution needed in the simulation

This section will detail the method we have used to estimate the required grid resolution in the computations. We first focus on the grid resolution requirements for the boundary layers of the nozzle flow. We start our analysis with the following equation which gives the radial or normal distance from the nozzle wall in wall units:

$$\Delta_r^+ = u_\tau \Delta_r / \nu_{\text{wall}} \quad (13)$$

where  $\Delta_r$  is the radial distance from the wall,  $u_\tau$  is the friction velocity,  $\nu_{\text{wall}}$  is the wall kinematic viscosity, and the superscript  $+$  denotes wall units. Now, assuming that the wall kinematic viscosity is the same as the reference kinematic viscosity for an isothermal flow, it can be shown that

$$\Delta_r^+ = \left( \frac{\Delta_r}{D_j} \right) \left( \frac{u_\tau}{U_j} \right) Re_D. \quad (14)$$

The first grid point off the wall is required to be at  $\Delta_r^+ \approx 1$ . To compute the grid spacing needed for this resolution, we first need to know the value of the friction velocity,  $u_\tau$ . The friction velocity, in turn,

depends upon the Reynolds number. An initial estimate of the skin friction velocity can be obtained from flat plate skin friction correlations or the mean velocity profile given by the Spalding law [43]. In our case, we obtained an initial estimate from the Spalding mean velocity profile. This preliminary value was found to be  $u_\tau/U_j \approx 0.0574$  for a boundary layer with thickness of about  $2 \times 10^{-2}D_j$  at  $Re_D = 100,000$ . We then performed a preliminary round nozzle flow computation at  $Re_D = 100,000$  to determine the more accurate value of the skin friction velocity. Only the flow inside the nozzle was computed. At the nozzle inlet, the boundary layer thickness is set to  $\delta_{\text{inlet}}/D_j \approx 2 \times 10^{-2}$ . A nozzle length of  $0.5D_j = 25\delta_{\text{inlet}}$ , which should be sufficiently long, was chosen. Nozzle inflow conditions were generated in the simulation using the procedure described earlier. The velocity field was initialized with the mean profile given by the Spalding law [43]. Random streamwise velocity fluctuations with a maximum amplitude of 10% of the reference velocity were added to the initial mean velocity profile. The mean velocity profile at the nozzle inlet was kept fixed and set to the Spalding mean velocity profile. Only the fluctuations were recycled and re-introduced at the inlet. The recycle station was chosen at the streamwise location where  $x/D_j = 0.2 \approx 10\delta_{\text{inlet}}$ , which should be sufficiently far away from the inlet. The boundary layer thickness at the recycling station reached a value  $\delta_{\text{recycle}}/D_j \approx 2.5 \times 10^{-2}$  and the friction velocity at this station was found to be  $u_\tau/U_j \approx 0.0485$ . The skin friction velocity decays slowly with increasing streamwise distance within the nozzle. Using the value of the skin friction velocity at the recycling station, we now see that in order to have  $\Delta_r^+ \approx 1$  for the first grid point off the wall for a nozzle flow at  $Re_D = 100,000$ , the radial or normal grid resolution on the wall has to be  $\Delta_r/D_j \approx 2 \times 10^{-4}$ .

For the LES of channel-type flows and turbulent boundary layers, a streamwise grid spacing of about 100 wall units and a spanwise grid spacing of about 20 wall units are typically recommended to resolve the inner layer eddies of the boundary layer [35]. Hence, for this kind of resolution, we see that the normalized streamwise grid spacing has to be  $\Delta_x/D_j \approx 2 \times 10^{-2}$ , while the normalized azimuthal grid spacing has to be  $\Delta_\theta/D_j \approx 4 \times 10^{-3}$ . In our study, our maximum streamwise grid spacing within the nozzle is  $\Delta_x/D_j = 6.78 \times 10^{-3}$ , or  $\Delta_x^+ \approx 33$  and the azimuthal grid spacing corresponds to  $\Delta_\theta^+ \approx 24$ . The streamwise grid spacing at the nozzle inlet is  $\Delta_x/D_j = 6.78 \times 10^{-3}$  and decreases towards  $\Delta_x/D_j = 2 \times 10^{-4}$  at the nozzle exit, where the streamwise grid spacing is essentially the same as the wall normal grid spacing. Hence, for the nozzle, 107 streamwise points and 639 azimuthal points are required. In the radial direction, there are about 45 points within the initial boundary layer at the nozzle inlet, and another 55 points outside the boundary layer within the annular grid. The core region of the nozzle is discretized by a rectangular grid as shown earlier. The first radial grid point off the wall is at  $\Delta_r^+ \approx 1$ . The coarsest radial grid resolution in the boundary layer corresponds to  $\Delta_r^+ \approx 13$ . To compare our boundary layer grid resolution with that used by Visbal and Rizzetta [51] in their study on the comparison of the ILES approach with explicit SGS models, their grid resolution in wall units was 47.1 in the streamwise direction and 23.4 in the spanwise direction. Their coarsest resolution in the wall-normal direction was 25.8. To re-iterate, with this resolution, Visbal and Rizzetta [51] demonstrated that the use of explicit SGS models does not give any better results than the ILES approach in the turbulent channel flow. Clearly, our streamwise and wall-normal direction resolutions are better than their corresponding resolutions while our azimuthal grid resolution is about the same as their spanwise grid resolution. Thus, we have confidence that our boundary layer resolution is sufficient for the ILES approach to be accurate in the boundary layer region.

Our goal is to capture the high frequency noise generation which takes place within the first three diameters of the nozzle exit, hence the truncation of the computational domain at four nozzle diameters downstream of the nozzle exit is a reasonable choice. In the region downstream of the nozzle, a streamwise grid spacing of  $\Delta_x/D_j \approx 2 \times 10^{-2}$  or  $\Delta_x^+ \approx 100$ , is expected to be sufficient to properly resolve the structures generating the noise in the bulk of the mixing layer. This resolution corresponds to roughly three times the coarsest resolution within the nozzle. Moreover, after an initial adjustment region, the size of the structures in the shear layer are expected to linearly increase with downstream distance. Thus, the chosen streamwise grid resolution for the shear layer seems appropriate. With this resolution, 50 streamwise points per diameter are required. A streamwise grid spacing of  $\Delta_x^+ \approx 50$  would be more desirable; however, this resolution doubles the grid points needed in the shear layer region. It should also be kept in mind that the streamwise grid resolution at the nozzle exit should be  $\Delta_x^+ = 1$  so that the transfer of the boundary layer turbulence into the jet shear layers will take place without any issues. The streamwise grid spacing at the nozzle exit should be the same as the wall-normal grid spacing. Taking all of these issues into account, we see that we need a total of about 353 streamwise points to cover the region from the nozzle inlet at  $x/D_j = 0$  to the streamwise location at  $x/D_j = 4.5$ . The first 107 points cover the region inside the nozzle where  $0 \leq x/D_j \leq 0.5$ . For the sponge zone of length  $3D_j$  to be attached downstream of the physical domain, another 40 streamwise grid points are needed. Hence, the total

number of streamwise grid points is 393. The number of grid points in the azimuthal direction is kept fixed at 639. The reader is reminded that there are about 45 radial points within the boundary layer at the nozzle inlet. The boundary layer thickens with increasing streamwise distance within the nozzle, thus, the number of radial grid points within the boundary layer at the nozzle exit is about 50. The boundary layers that separate at the nozzle exit form the shear layers of the free jet flow. The width of the shear layer (or the mixing zone) of the jet increases with the downstream distance. Schlichting [40] provides the following velocity profile solution for the mixing zone of an incompressible jet with zero co-flow:

$$\frac{u}{U_j} = \frac{1}{2} \left\{ 1 + \operatorname{erf} \left( \sigma \frac{(r_{\text{lip}} - r)}{x} \right) \right\}, \quad (15)$$

where  $\operatorname{erf}$  is the error function,  $\sigma = 13.5$ ,  $r_{\text{lip}}$  is the radial location of the nozzle lip line (that is,  $r_{\text{lip}} = 0.5D_j$  in our case) and  $x$  is the downstream distance measured from the nozzle exit. This velocity profile can be used to estimate the mixing region width at a given downstream location. However, for compressible jets, it is known that the mixing zone becomes somewhat narrower with increasing Mach number. The Mach number of the isothermal jet simulated in the current study is 0.6 and the corresponding convective Mach number is 0.3. The compressibility effects at this convective Mach number are not expected to be significant, hence the above profile can still be used to estimate the width of the mixing zone. According to this equation, at 4 diameters downstream of the nozzle exit, we see that  $u/U_j = 0.01$  at  $r/D_j \approx 0.987$  and  $u/U_j = 0.99$  at  $r/D_j \approx 0.013$ . Thus, the width of the mixing region at this downstream location is almost one diameter.

At the nozzle exit, we have 100 grid points in the radial direction within the nozzle. These points cover the region  $0.15 \leq r/D_j \leq 0.5$ . The core region is discretized by a relatively coarse rectangular grid as previously shown in Fig. 1. At the nozzle exit, roughly half of the radial grid points are located within the nozzle boundary layer. We wish to have a more uniform radial grid distribution at the station  $x/D_j = 4.5$ . The radial grid point distribution can be adjusted with downstream distance for this purpose. At  $x/D_j = 4.5$ , the mixing zone extends to about  $r/D_j = 0.987$  from the previous analysis. The edge of the mixing zone is approximately half a diameter “above” the nozzle lip line.

The thickness of the nozzle lip is set to  $10^{-2}D_j$ . There are 42 points within the nozzle lip at the nozzle exit. The lip-line grid expands with downstream distance as shown in Figs. 2 and 3. The side grid encloses the nozzle geometry and the lip-line grid as also shown in the figures. This grid covers the intermediate region in between the shear layers where noise is generated and the outside region where linear acoustic wave propagation takes place. The streamwise grid spacing of the side grid exactly matches that of the lip-line grid in the region downstream of the nozzle exit. The side grid has 50 points upstream of the nozzle exit. The maximum streamwise spacing in that section is  $3 \times 10^{-2}D_j$ . Hence, there are 331 streamwise grid points total in the side

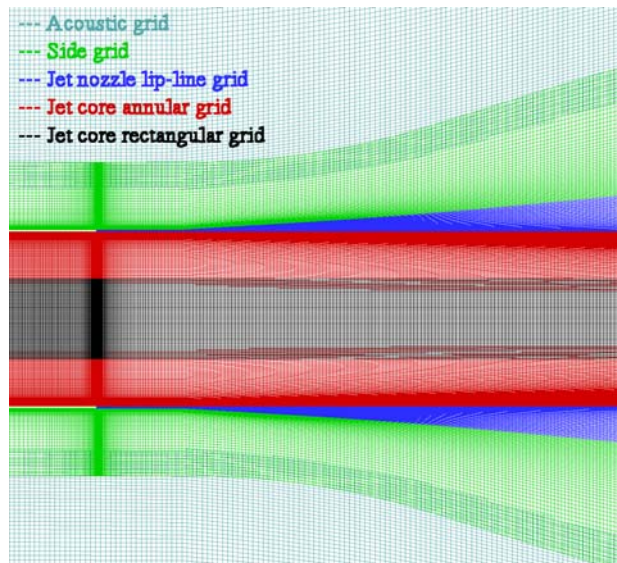


**Fig. 2** Grids in the vicinity of the nozzle exit. White strips denote nozzle walls



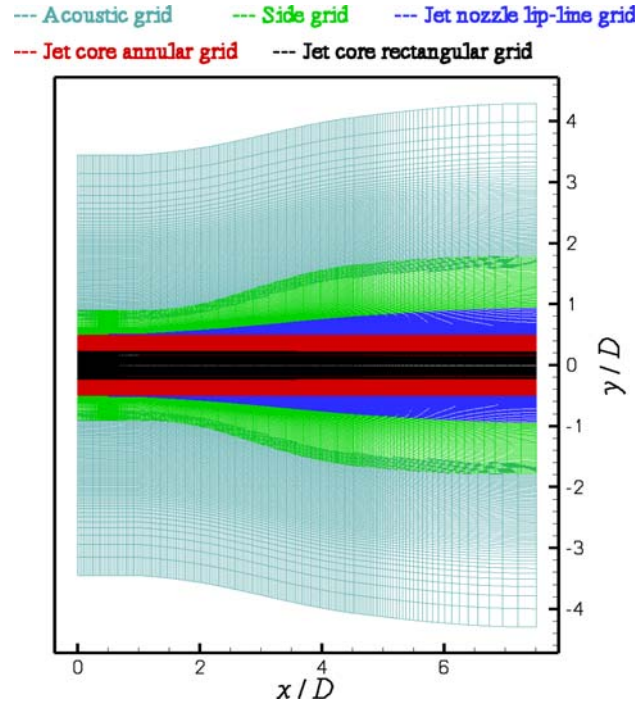


Fig. 3 Another look at the grids used in the simulation

Table 1 Grid information

Component grid name	Streamwise points	Radial points	Azimuthal points	Grid points	Unused points	Interpolation points	Number of blocks
Jet core rectangular grid	393	N/A	N/A	1, 022, 193 (=393 × 51 × 51)	266,876	205,860	6
Jet core annular grid	393	100	639	25, 112, 700	0	752,202	126
Jet nozzle lip-line grid	287	42	639	7, 702, 506	0	0	45
Side grid	336	54	639	11, 594, 016	0	643,104	54
Acoustic grid	195	80	319	4, 976, 400	594,597	196,842	25
Total				50,407,815	861,473	1,798,008	256

grid. The radial grid distributions within the jet core cylindrical grid, lip-line grid and the side grid provide a total of 90–100 radial grid points across the mixing region in the jet shear layers.

Finally, we have an acoustic grid which encloses the side grid. The acoustic grid is fine enough to resolve frequencies of up to Strouhal number of about 20 in the near acoustic field region just outside the shear layers. The radial grid spacing in the vicinity of the FWH control surface, which lies within the acoustic grid, is  $\Delta_r/D_j \approx 0.02$ . This gives the estimate of a cut-off Strouhal number of around 20 assuming that the compact scheme we are using needs at least four points per wavelength to accurately resolve an acoustic wave. The number of azimuthal grid points in the acoustic grid is half of that in the other three annular grids. The streamwise grid spacing of the acoustic grid is uniform in the physical portion of the domain and equal to  $2.9 \times 10^{-2} D_j$ . The acoustic grid and the side grid communicate by means of the high-order interpolation procedure mentioned earlier. The acoustic grid is stretched along the radial direction towards the lateral boundary and also along the streamwise direction within the sponge zone to dissipate the acoustic waves before they reach the boundaries. All grids contain a sponge zone whose streamwise length is three diameters beyond the end of the physical domain. Grid stretching and application of non-reflecting boundary conditions on the outer domain boundaries minimize unwanted numerical reflections back into the domain.

Table 1 summarizes the information about the grids used in the simulation. The “Grid points” column in the table shows the total number of grid points in every component grid prior to removing the excess grid overlap. The “Unused points” column gives the number of unused points after the excess grid overlap is removed by OGEN [23] and the “Interpolation points” column shows the total number of interpolation points for every

grid. The last column shows the number of blocks into which every component block has been partitioned for parallel computing. The total number of discretization points at which the governing equations must be solved is almost 50 million. The five grids are partitioned into 256 blocks total.

## 4 Test case: simulation of the near-nozzle region of a Mach 0.6 Jet

### 4.1 Simulation details

We present results from the simulation of a Mach 0.6 isothermal jet exhausting from a round nozzle configuration. The Reynolds number based on the jet nozzle exit centerline velocity and nozzle diameter,  $Re_D$ , is set to 100,000. The nozzle length is  $0.5D_j$ , while the nozzle lip thickness is  $10^{-2}D_j$ . The jet temperature is the same as the ambient temperature and is set to 300K. A boundary layer thickness of  $\delta_{inlet}/D_j = 2 \times 10^{-2}$  is specified at the nozzle inlet. The boundary layer thickness at the nozzle exit reaches a value of  $\delta_{exit}/D_j \approx 3 \times 10^{-2}$  with a corresponding momentum thickness of  $\delta_\theta/D_j \approx 3 \times 10^{-3}$ . While our nozzle exit boundary layer thickness is certainly smaller than that in most other jet noise calculations, the nozzle exit boundary layers in practical jet noise applications are even thinner. The difficulty of calculating realistically thin boundary layers has been recognized as one of the main issues in jet simulations (see, for instance, the review of Bodony and Lele [12]).

Characteristic viscous wall boundary conditions [26] are applied at the nozzle walls. Adiabatic boundary conditions are additionally imposed on all walls. Although temperature is not one of the solution variables, it is related to density and pressure through the ideal gas relation. Adiabatic wall boundary conditions are enforced by setting the heat flux term in the wall normal direction to zero in the energy equation. Characteristic-type inflow boundary conditions [25] are applied on the inlet of the side grid and the acoustic grid. Although zero co-flow conditions are used in the present simulation, use of characteristic-type boundary conditions on the inlet plane of these grids enables the application of non-zero co-flow conditions while allowing the upstream traveling acoustic waves cross this boundary without spurious reflection back into the domain. Tam and Dong radiation boundary conditions modified by Dong [18] are applied on the lateral boundary of the acoustic grid. Characteristic-type outflow boundary conditions [25] are applied at the end of the sponge zone in all grids. Nozzle inlet boundary conditions are generated using the rescaling–recycling procedure mentioned earlier. The recycle station was chosen at the streamwise location where  $x/D_j = 0.2 = 10\delta_{inlet}$ . The nozzle inlet is at  $x/D_j = 0$  and the nozzle exit is at  $x/D_j = 0.5$ .

The simulation has been performed with implicit time stepping. Two sub-iterations were applied per time step. The filtering parameter was set to  $\alpha_f = 0.47$ . The computational time step is  $\Delta t = 10^{-3}D_j/U_j$  and corresponds to  $\Delta t^+ = \Delta t u_\tau^2/\nu_{wall} \approx 0.235$  in wall units. It is known that the viscous time scale or the Kolmogorov time scale, which is the smallest time scale of turbulence, in a turbulent boundary layer is  $O(1)$  in wall units [14]. Thus, to ensure that the time scales in the nozzle boundary layers are properly resolved, we set our computational time step to be less than the viscous time scale. With this time step, 1,000 time steps are required for a particle moving at the jet nozzle exit centerline velocity to travel one nozzle diameter. Also, with the current time step, we see that there are 50 temporal points in one period of an acoustic wave with a frequency of Strouhal number 20. Strouhal number 20 corresponds to the upper limit of the frequency range that we hope to capture in the current computation. Although the computational grids are fine enough to support the propagation of acoustic waves with very high frequencies, the question of whether the turbulence length scales responsible for the generation of such high frequencies are active in the present simulation will have to wait for an answer until the far field noise spectra are analyzed.

The simulation was run for a total of 112,150 time steps. The first 46,800 time steps were used to drive the initial numerical transients out of the computational domain. The unsteady flow data computed over the next 65,350 time steps were used for the flow statistics, far field noise calculations via the Ffowcs Williams–Hawkings method and the two-point space-time correlations within the jet shear layers. The sampling period corresponds to a time scale of  $65.35D_j/U_j$  or  $108.92D_j/c_\infty$ . Most of the simulation was performed using 256 processors in parallel on the NCSA Xeon Linux Cluster (*Tungsten*) [1]. A small portion of the computation was run using 256 processors on the Cray XT3 machine (*Bigben*) [2] at the Pittsburgh Supercomputing Center. About 18 days total run time is needed on *Tungsten* for the whole simulation. We should note that the code runs about 25% faster on *Bigben*.

The cylindrical FWH control surface on which certain quantities are integrated for the prediction of far field noise has an initial radius of about one nozzle diameter near the inlet boundary at  $x/D_j = 0$ . The control surface extends to the end of the physical domain where  $x/D_j = 4.5$ . The radius of the surface at this location



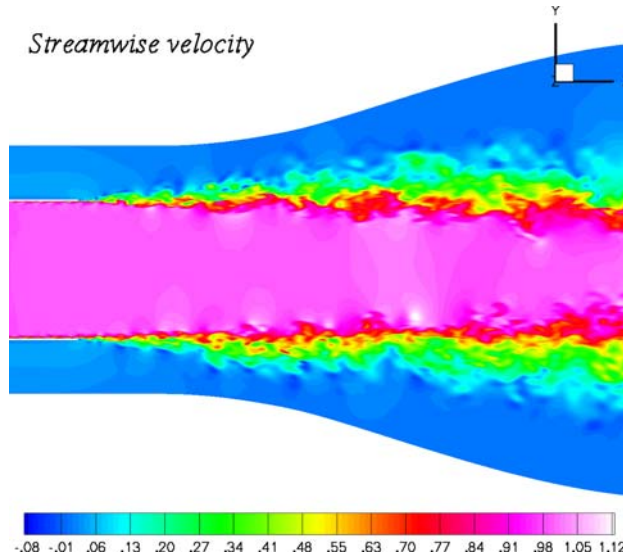


**Fig. 4** Contours of non-dimensional instantaneous streamwise velocity on the  $xy$  plane

is equal to approximately  $1.67D_j$ . The control surface lies within the acoustic grid shown earlier and coincides with a grid surface plane on which the radial grid index is held constant. Thus, the unsteady data needed in the surface integrals are directly provided to FWH surface integrals without any need for interpolation. To reiterate, the radial grid spacing in the vicinity of the FWH control surface is  $\Delta_r/D_j \approx 0.02$ . The FWH control surface is an open surface, meaning that the inlet and exit planes are not included in the integrals. In a study done on the use of open control surfaces in flow generated noise applications, Freund et al. [21] indicate that for an open control surface, if the straight line between the source and the observer goes through part of the surface, then the result is acceptable; however, if the line goes through the open part, then the result is erroneous. In this problem, we are only interested in computing the high frequency noise that propagates in the sideline direction, thus the open FWH control surface we use here captures the noise in this direction with sufficient accuracy. High frequency noise gets generated within the first few nozzle diameters downstream of the nozzle exit and our FWH control surface is long enough to enclose this region.

## 4.2 Simulation results

### 4.2.1 Flow visualization

We first show a few flow visualization pictures to depict the nature of the jet shear layers. Figure 4 plots the non-dimensional instantaneous streamwise velocity contours on the  $xy$  plane that cuts the jet in half, whereas Figs. 5, 6, 7, and Fig. 8 plot the contours of instantaneous streamwise velocity on four planes downstream of the nozzle where  $x/D_j = 1, 2, 3, 4$ , respectively. As can be seen from the pictures, the shear layers are certainly not laminar downstream of the nozzle exit. As expected, the shear layer thickens with increasing downstream distance. A snapshot of the instantaneous vorticity in the jet shear layers and the high frequency noise radiation is provided in Fig. 9. Note that some of the acoustic waves seem to have their origins immediately downstream of the nozzle exit. As we will see later, we believe that the initial state of the jet shear layer, which is transitional, results in noise generation due to vortex pairing in that region.

Figure 10 visualizes the state of the nozzle boundary layer by depicting the instantaneous streamwise velocity contours on a cylindrical shell that is located at about 33 wall units from the nozzle wall. On this plane, we see high-speed fluid streaks which are denoted by red and purple. In between these fast-moving streaks, we also observe relatively slower moving streaks denoted by shades of green and blue. This shows that the boundary layer is certainly not laminar. Although similar observations have been made in experimental turbulent boundary layers, this observation alone is not sufficient to accurately conclude that the boundary layer within the nozzle is fully turbulent. The boundary layer might also be in a transitional state. Quantitative analysis presented in the following sections will be more helpful towards a more accurate determination of the boundary layer state.

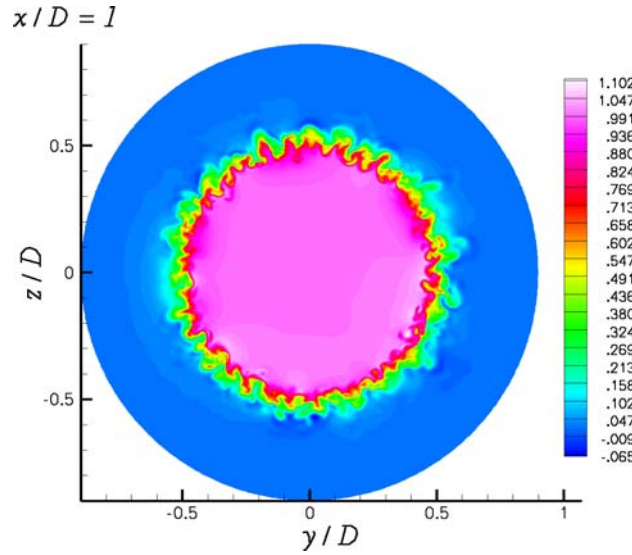


**Fig. 5** Contours of non-dimensional instantaneous streamwise velocity on the plane where  $x/D_j = 1$

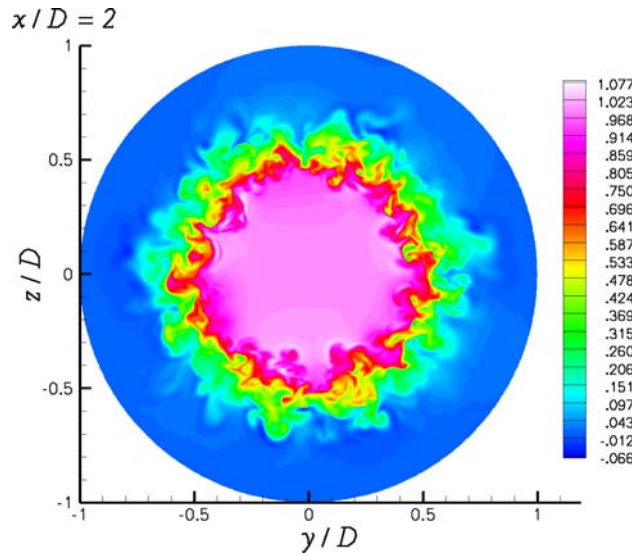


**Fig. 6** Contours of non-dimensional instantaneous streamwise velocity on the plane where  $x/D_j = 2$

#### 4.2.2 Turbulence statistics and mean flow

Next, we examine the properties of the boundary layer near the nozzle exit, more precisely at the location where  $x/D_j \approx 0.497$ , which is slightly upstream of the separation location at  $x/D_j = 0.5$ . Figure 11 plots the normalized mean streamwise velocity profile. Here,  $U^+$  and  $\Delta r^+$  represent the mean streamwise velocity and the normal distance from the nozzle wall, respectively, in wall units. As can be seen from the figure, the profile agrees with the linear equation,  $U^+ = \Delta r^+$ , very well in the viscous sublayer region. The figure also plots the logarithmic layer curve,  $U^+ = (1/\kappa) \ln(\Delta r^+) + C$ , where  $\kappa = 0.41$  and  $C = 5$ . The log layer is defined as the region that lies between the viscous sublayer and the defect layer of a turbulent boundary layer. However, our mean profile does not appear to have a log layer at all. The lack of the log layer can be explained by the relatively low Reynolds number based on momentum thickness,  $Re_\theta$ , which is approximately 300 near the nozzle exit. In his direct numerical simulation of turbulent boundary layers up to  $Re_\theta = 1410$ , Spalart [42] did not observe a log layer for a turbulent boundary layer at  $Re_\theta = 300$  either. From Spalart's argument, it appears that the log layer simply disappears at low enough values of  $Re_\theta$ . On the other hand, even though

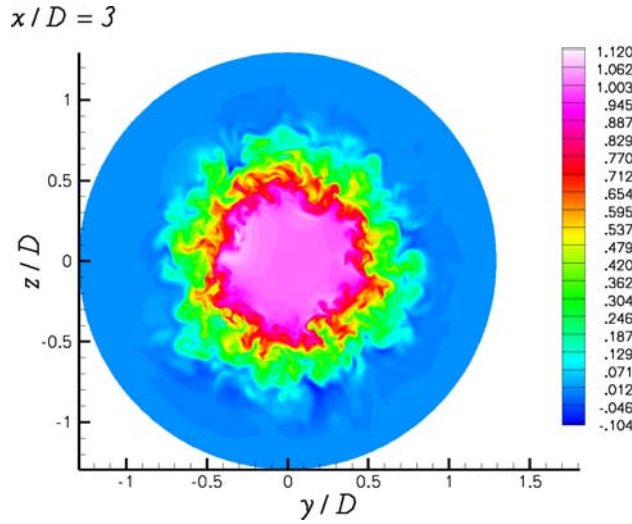


**Fig. 7** Contours of non-dimensional instantaneous streamwise velocity on the plane where  $x/D_j = 3$

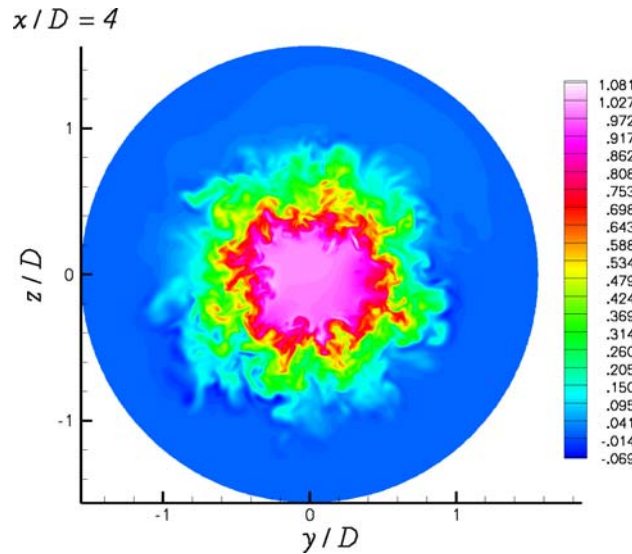


**Fig. 8** Contours of non-dimensional instantaneous streamwise velocity on the plane where  $x/D_j = 4$

the low  $Re_\theta$  explains the lack of a log layer, it does not explain the large velocity overshoot above the log law. It turns out that the velocity profile shown here is actually representative of a transitional rather than a fully turbulent boundary layer. In a study done by Rai and Moin [37] on the DNS of transition and turbulence in a spatially evolving boundary layer, the shape of the velocity profile of the boundary layer at various stages during transition from laminar to turbulent state was clearly demonstrated. They have shown that a boundary layer in the transitional stage clearly has a large overshoot above the log law, similar to what is observed here. Thus, the velocity profile shown here is quite similar to those of transitional boundary layers in the study of Rai and Moin [37]. This is the first evidence for the transitional state of our nozzle exit boundary layer.

The shape factor of the boundary layer, which is the ratio of the displacement thickness to momentum thickness, near the nozzle exit has been found to be about 1.71 in the computation. For a laminar boundary layer with a Blasius velocity profile, the shape factor value is about 2.6, whereas values close to 1.4 are typically found in turbulent boundary layers. Values in between 2.6 and 1.4 are expected for transitional boundary layers. Since our shape factor is not exactly 1.4, this can be used as the second evidence for the transitional state of the nozzle exit boundary layer.

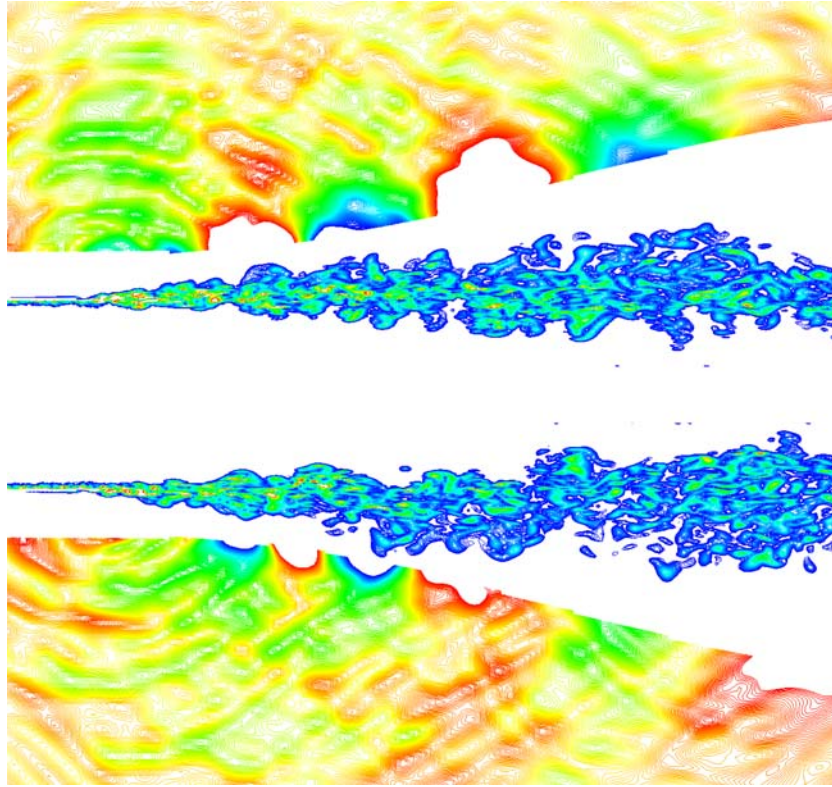
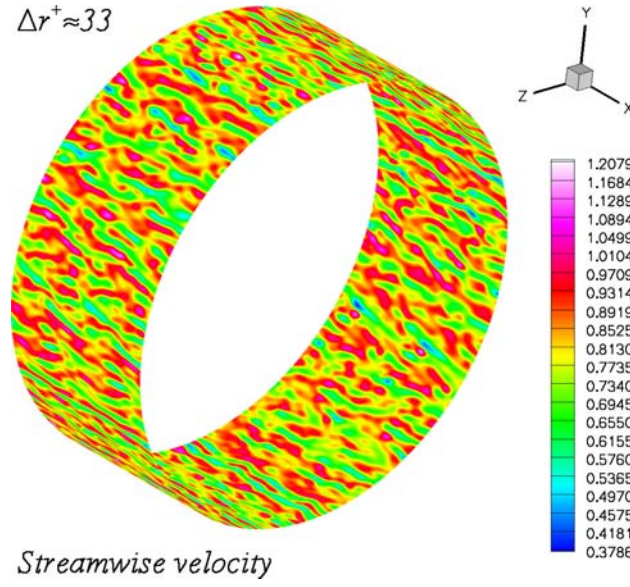


**Fig. 9** Contours of instantaneous vorticity in the jet shear layers and the instantaneous pressure field depicting noise radiation from the shear layers

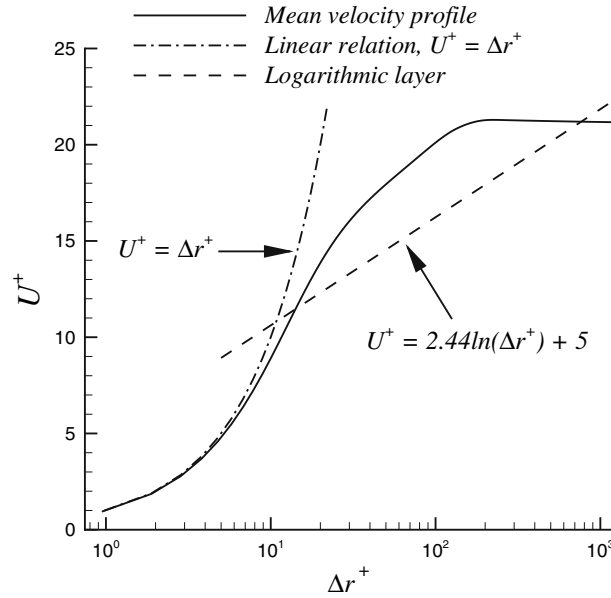
Figure 12 plots the streamwise, radial and azimuthal turbulence intensities near the nozzle exit, again at the location where  $x/D_j \approx 0.497$ . The intensities are normalized by the wall friction velocity,  $u_\tau$  at the given location. The DNS profiles from Spalart's turbulent boundary layer calculations at  $Re_\theta = 300$  [42] are also shown in the same figure for comparison. Our azimuthal turbulence intensity profile displays the best agreement with the spanwise turbulence intensity profile of the DNS, while our other two profiles have good overall qualitative agreement with the corresponding DNS profiles. Going back to our profiles, we see that the peak streamwise turbulence intensity is much larger than the peaks of the other two components. The streamwise turbulence intensity peaks very near the wall, where  $\Delta r^+ \approx 17$ . The profile peak is within one displacement thickness. The azimuthal intensity reaches its peak value at  $\Delta r^+ \approx 30$ , while the radial turbulence intensity reaches its peak value at  $\Delta r^+ \approx 65$ . The edge of our boundary layer is at  $\Delta r^+ \approx 200$ .

Figure 13 plots the streamwise turbulence intensity and the mean streamwise velocity variation along the nozzle lip line. Both the streamwise turbulence intensity and the mean streamwise velocity are normalized by the reference velocity,  $U_j$ . The normalized streamwise velocity is zero on the nozzle wall at the nozzle exit, and increases to a value slightly larger than 0.6 within several nozzle diameters. The velocity profile then stays almost constant with increasing downstream distance. The normalized streamwise turbulence intensity profile initially displays a rapid increase to a large value immediately downstream of the nozzle exit. We believe this overshoot is caused by the initial instability of the shear layer and the subsequent formation of energetic vortices at the instability frequency. This point will be discussed in more detail shortly. After the initial overshoot, the turbulence intensity profile decays to its asymptotic value of about 0.135 at around 3.5 or 4 nozzle diameters downstream of the nozzle exit. It should be noted here that shear layers with fully turbulent initial conditions do not display such initial overshoots in the turbulence intensity profile [11]. Initially laminar shear layers, however, are known to display such initial overshoots [11]. We are not aware of any experimental study of an initially transitional shear layer, thus it is hard to tell at this point whether such a shear layer will also have an initial overshoot. Nevertheless, one would expect that the behavior of an initially transitional shear layer would fall somewhere between that of an initially laminar shear layer and an initially turbulent shear layer. So, perhaps there should be an overshoot in the case of a initially transitional shear layer as well. Previous





**Fig. 10** Contours of non-dimensional instantaneous streamwise velocity on a cylindrical surface where  $\Delta r^+ \approx 33$  in the nozzle boundary layer



**Fig. 11** Normalized mean streamwise velocity profile (in wall units) of the nozzle boundary layer near the exit

flow visualization figures clearly show that our shear layer is certainly not initially laminar and the presence of an initial overshoot in the turbulence intensity along the nozzle lip line suggests it is not fully turbulent. This implies that our shear layer must be in an intermediate, i.e. transitional stage. This is the third evidence for the transitional state of our nozzle exit boundary layer.

#### 4.2.3 Turbulence length and time scales along the nozzle lip line

To compute the turbulence length and time scales in the streamwise, radial, and azimuthal directions in the middle of the mixing layer, we can make use of the two-point velocity correlations along the nozzle lip line where  $r = 0.5D_j$ . The integral length scale,  $L(x_o)$ , which approximately represents the size of the large or the most energetic length scale in a particular direction at the given streamwise location  $x = x_o$ , can be calculated

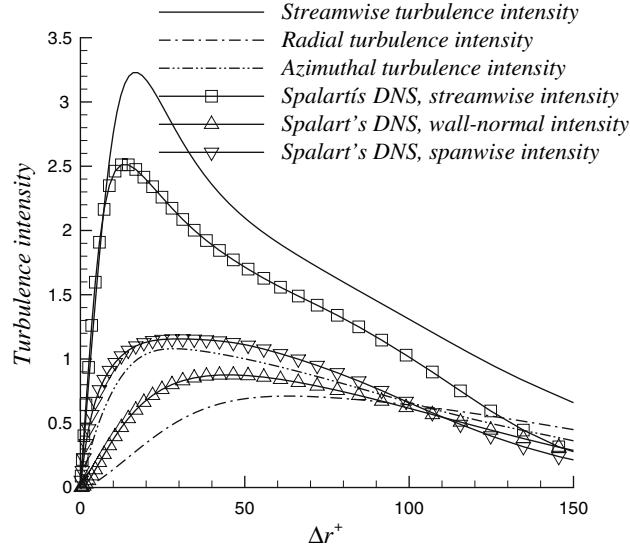


**Fig. 12** Normalized turbulence intensity profiles (in wall units) of the nozzle boundary layer near the exit

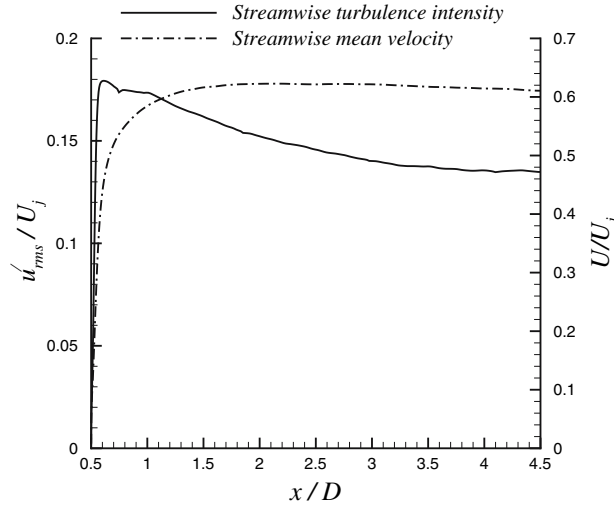


**Fig. 13** Turbulence intensity and mean velocity along the nozzle lip line

by computing the area under the two-point velocity correlation curve. For example, the two-point velocity correlation in the streamwise direction at  $x = x_o$  is defined as

$$\mathcal{R}_{xx}(x_o, \xi, t) = \frac{\langle u'(x_o, t)u'(x_o + \xi, t) \rangle}{\langle u'(x_o, t)u'(x_o, t) \rangle}, \quad (16)$$

where  $\xi$  represents the spatial separation between the two points. On the other hand, the streamwise velocity scale of the large eddy can be taken as the local streamwise turbulence intensity. Hence, to estimate the corresponding time scale in the streamwise direction,  $\tau(x_o)$ , we can simply use the relation  $\tau(x_o) = L(x_o)/u'_{\text{rms}}(x_o)$  from dimensional analysis. Similar relations are defined to estimate the length and time scales in the radial and azimuthal directions. It should be kept in mind that since there is a certain amount of energy in the unresolved scales, the computed integral length scales and the corresponding time scales should be taken as estimates only. Since no explicit subgrid-scale modeling is used in the present computations, it is hard to estimate the amount of energy in the unresolved scales.

Figures 14, 15, and 16 plot the two-point velocity correlations along the three spatial directions at certain streamwise locations. As can be seen from the figures, all correlations decay very rapidly in the region



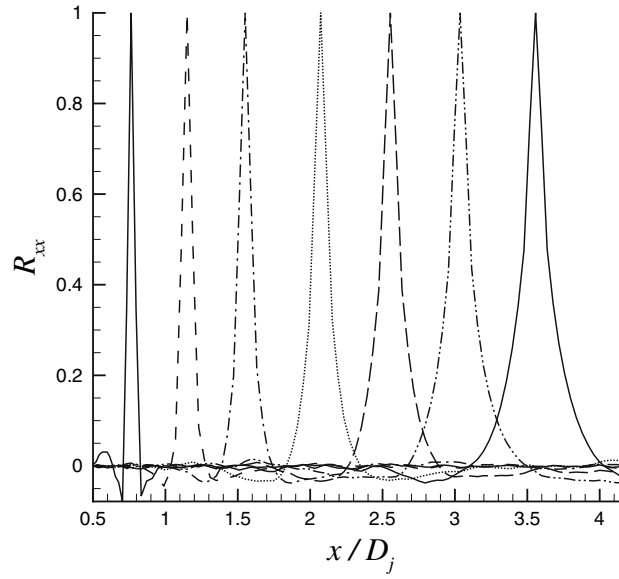


**Fig. 14** Two-point streamwise velocity correlations ( $\mathcal{R}_{xx}$ ) at several locations along the nozzle lip line

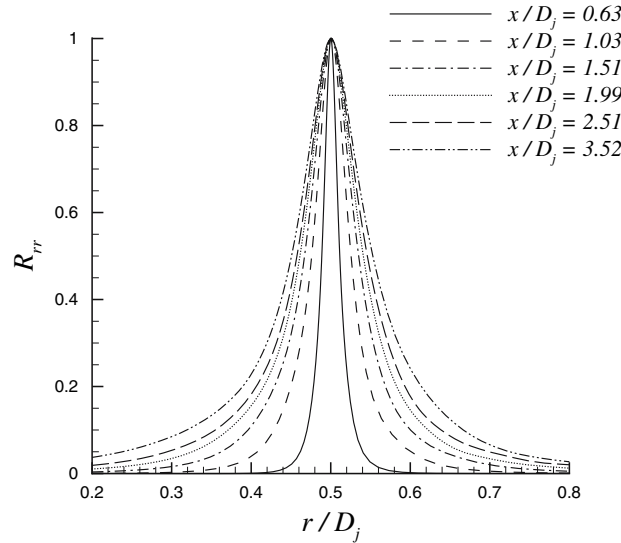
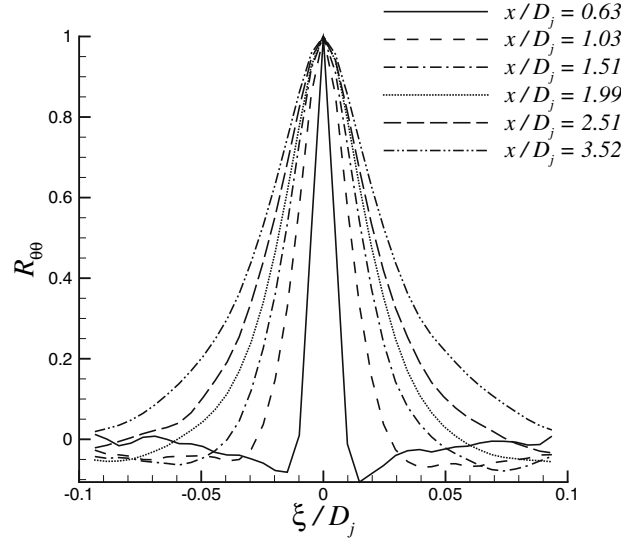


**Fig. 15** Two-point radial velocity correlations ( $\mathcal{R}_{rr}$ ) at several locations along the nozzle lip line

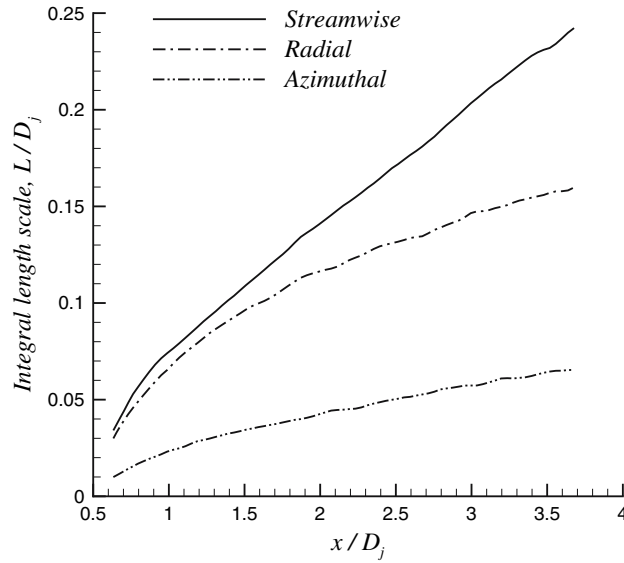
immediately downstream of the nozzle exit, meaning that the length scales are very small in this region. The correlations get wider with increasing downstream distance, implying that the length scales are becoming larger with increasing downstream distance. This is expected for a mixing layer.

Figure 17 plots the three integral length scale variations along the nozzle lip line. As was already evident from the two-point velocity correlations, the length scales become larger with increasing downstream distance. After an initial region near the nozzle exit, which appears to be an adjustment region, all length scales seem to increase in size almost linearly. The small wiggles observed in the curves are due to the limited statistical sample size. It is also observed that at any given downstream location, the azimuthal length scale is the smallest of the three length scales, while the streamwise length scale is the largest. This agrees well with the observation made by Townsend [44].

Figure 18 depicts the eddy turnover frequency (or the inverse eddy turnover time) of the large scales along the nozzle lip line. The eddy turnover frequency is simply equal to the inverse of the time scale of the large scales. As can be seen from the figure, the azimuthal frequency is the largest of the three frequencies at all



**Fig. 16** Two-point azimuthal velocity correlations ( $R_{\theta\theta}$ ) at several locations along the nozzle lip line



**Fig. 17** Integral length scales along the nozzle lip line

locations. Moreover, the azimuthal frequency is very high immediately downstream of the nozzle exit. All frequencies decay with downstream distance.

#### 4.2.4 Spectra of velocity fluctuations

To provide more evidence for vortex pairing, which we will discuss in more detail when we examine far field noise results, we first examine some velocity spectra in the region immediately downstream of the nozzle exit. Figure 19 plots the spectra of the streamwise velocity fluctuations at three streamwise locations in this region. These spectra are taken along a line that lies within the shear layer. The radial distance between this line on which spectra are taken and the nozzle wall lip line is around  $3 \times 10^{-2} D_j$ , which is about the same as the nozzle exit boundary layer thickness. Basically, these spectra are taken near the interface between the shear layer and the high-speed jet flow. As can be seen from the figure, the spectral peaks are clearly present at the two locations closest to the nozzle exit. All peaks disappear at the third location, which is located at  $x/D_j = 0.91$ . The first peak in the two spectra closest to the nozzle exit is at around  $Sr_D \approx 4.15$ , which is

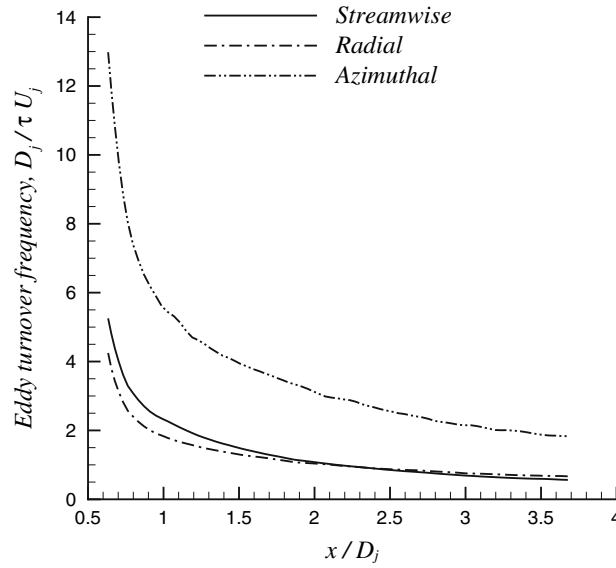


**Fig. 18** Eddy turnover frequency of the large scales along the nozzle lip line

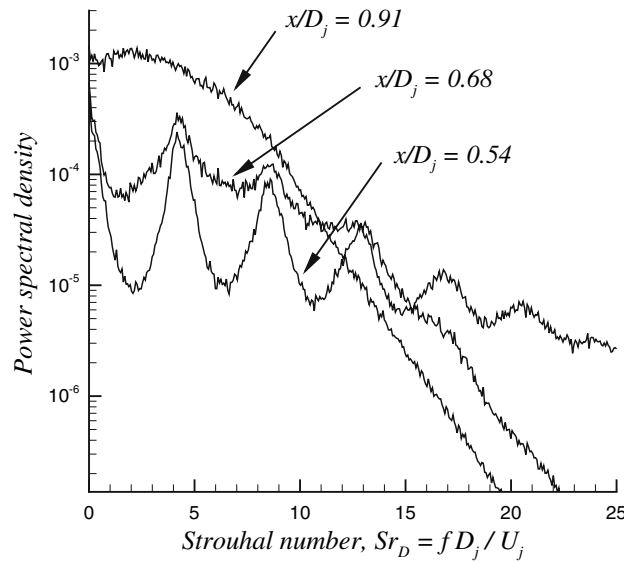


**Fig. 19** Spectra of the streamwise velocity fluctuations at three locations within the shear layer in the near-nozzle region. The radial distance between the spectra measurement points and the nozzle wall lip line is about  $3 \times 10^{-2} D_j$

believed to be the vortex pairing frequency. This will be discussed in more detail later. The spectrum closest to the nozzle exit displays four other clear peaks and a rather weak fifth one. The frequencies of these secondary peaks are approximately two, three, four and five times the frequency of the first peak, respectively, meaning that these peaks must be the harmonics of the fundamental frequency at  $Sr_D = 4.15$ . We will observe similar peaks in the noise spectra in the sideline direction when we examine the far field noise of the jet. The spectrum at the second location, where  $x/D_j = 0.68$ , has 3 clear peaks and it appears the peaks at the higher harmonics have disappeared at this location. As demonstrated by the experimental study of Bridges and Hussain [13], a jet with initially laminar shear layers, which does have additional noise generation due to vortex pairing in the shear layer, has similar shear layer velocity spectra with spectral peaks in the near-nozzle region.

Figures 20, 21, and 22 show the spectra of streamwise, radial and azimuthal velocity fluctuations at three streamwise locations on the lip line, further downstream of the nozzle exit. The figures verify the existence of broadband spectra for all components of the velocity fluctuation at the given locations. As expected, the high

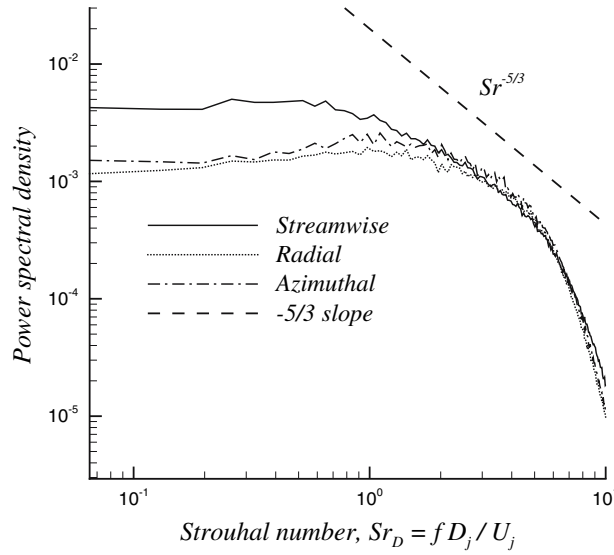


**Fig. 20** Spectra of the streamwise, radial and azimuthal velocity fluctuations on the lip line at  $x/D_j = 2$

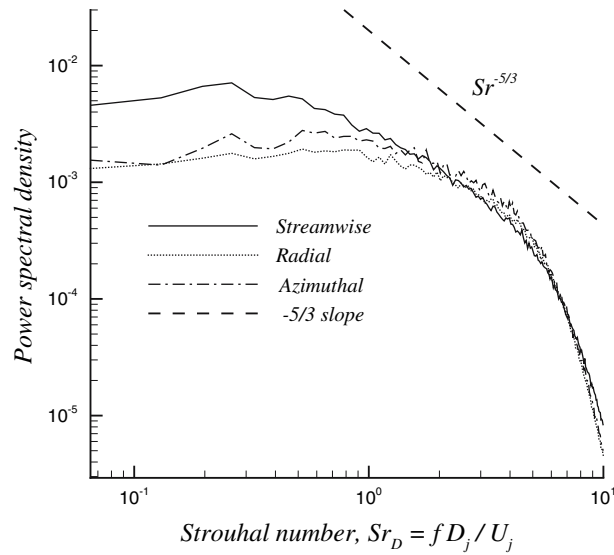


**Fig. 21** Spectra of the streamwise, radial and azimuthal velocity fluctuations on the lip line at  $x/D_j = 3$

frequencies, which correspond to the small scales, have much less energy than the low frequencies, which correspond to the large scales. The inertial range, in which the spectrum decay rate predicted by Kolmogorov is about  $-5/3$ , is rather narrow in the streamwise spectra at the first two locations, while it seems to be a bit wider at the third location. The existence of an inertial range in the radial and azimuthal spectra is not quite evident. The reason for this behavior of the spectra might be the fact that since the shear layer does not exactly start out with a fully turbulent state, as discussed earlier, the flow may still be not fully turbulent for some distance downstream of the nozzle exit. The spectra decay much faster beyond  $Sr_D \approx 6$ , indicating the approximate location of the grid cut-off Strouhal frequency at these locations. The low frequencies of the streamwise velocity fluctuations are observed to be more energetic than those of the other two components.

#### 4.2.5 Far field noise in the sideline direction

The far field noise will be examined next. Since high frequency noise is most dominant in the sideline direction, that is, at 90 degrees perpendicular to the jet axis, we will analyze the noise spectrum at this location. The

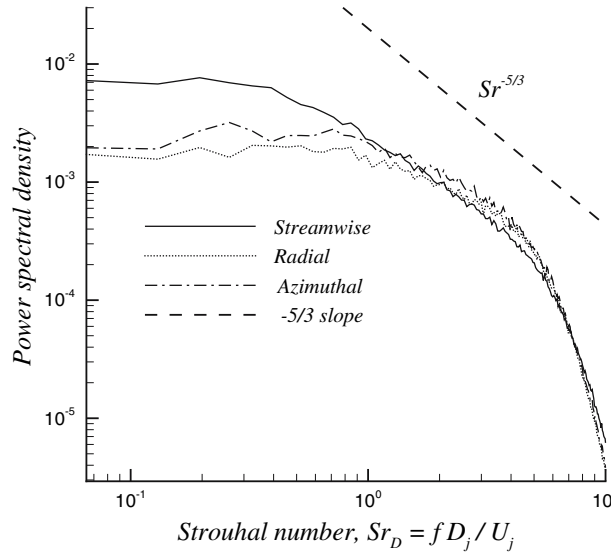


**Fig. 22** Spectra of the streamwise, radial and azimuthal velocity fluctuations on the lip line at  $x/D_j = 4$

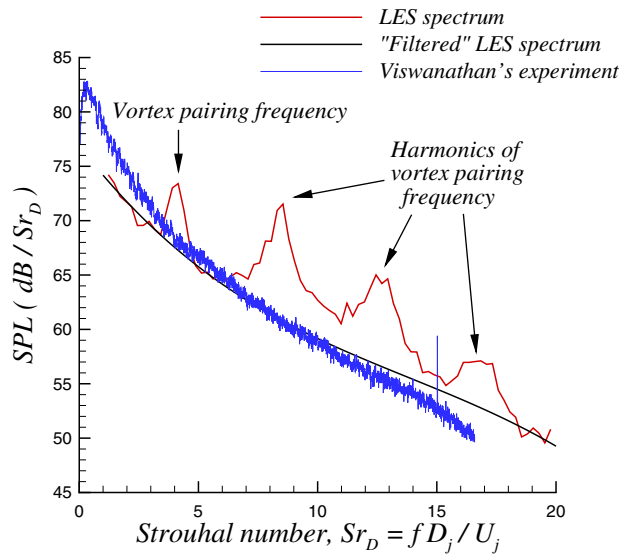


**Fig. 23** Far field sideline noise spectra at  $72D_j$  away from the nozzle exit centerline

observer at this 90-degree angle is located 72 nozzle diameters away from the jet nozzle exit. Since we are dealing with an axisymmetric problem, far field acoustic pressure signals were computed on the fly using the FWH method at 12 observer points that are uniformly distributed on a circle whose radius is equal to  $72D_j$ . The center of the circle is the same as the jet centerline at nozzle exit. The noise spectra computed at these 12 observer points were averaged to get the final averaged spectrum in the sideline direction.

Figure 23 shows the noise spectrum and compares it with the experimental spectrum of an unheated Mach 0.6 jet studied by Viswanathan [52]. The estimated Reynolds number of the experimental jet is about half a million, which is five times the LES Reynolds number. Frequencies less than about Strouhal number 1 are not well resolved in the simulation since those frequencies are mostly generated in the far downstream region, which our computational domain does not include. An interesting feature of the LES spectrum is that it displays broadband peaks at multiple frequencies. The first and the most energetic one is at around  $Sr_D = 4.15$ . Interestingly, the other spectral peaks are at approximately two, three and four times this frequency, respectively, meaning that these peaks must be the harmonics of the fundamental frequency at  $Sr_D = 4.15$ . We believe this

frequency corresponds to the frequency of the vortex pairing process that takes place in the initial region of the free shear layer. Velocity spectra were previously shown in this region to support the presence of vortex pairing. The velocity spectra in this region also had peaks at the same fundamental frequency and its harmonics.

The issue of “surplus” noise generation due to vortex pairing deserves some more discussion at this point. Previous research has shown that jets with initially turbulent shear layers do not have such peaks in the noise spectra. However, jets with initially laminar shear layers, do indeed display such peaks due to vortex pairing in the noise spectra. For example, Bridges and Hussain [13] have observed similar spectral peaks caused by vortex pairing for jets with initially laminar and thin shear layers. The momentum thickness Reynolds number,  $Re_\theta$  at the nozzle exit for the laminar jets they studied varied from 304 to 481. Moreover, they also demonstrated that the vortex pairing noise disappears when the boundary layers are tripped. The tripped boundary layers are turbulent and much thicker than laminar boundary layers. The momentum thickness Reynolds number at the nozzle exit for the turbulent jets they studied varied from 713 to 1,435. Vortex pairing noise in jets with initially laminar shear layers has also been demonstrated by Zaman [56].

We are not aware of any experimental study that focused on the noise of a jet with initially transitional shear layers. However, as was shown previously, the turbulence intensity variation in our shear layer is quite similar to that in an initially laminar shear layer. This means that our shear layer acts more or less like an initially laminar shear layer. The natural instability frequency of an initially laminar shear layer is  $Sr_\theta \approx 0.012 - 0.013$ , where  $Sr_\theta$  is the Strouhal number based on the initial momentum thickness of the shear layer. This is the formation frequency of vortices in an unforced, initially laminar shear layer. On the other hand, according to the experimental study of Hussain and Zaman [24], an initially turbulent plane mixing layer rolls up at a frequency of  $Sr_\theta \approx 0.024$ . In this case,  $Sr_\theta$  is the formation frequency of organized structures in an unforced, initially turbulent plane mixing layer. The experimental work conducted by Drubka [19] also confirms the existence of the instability frequency at  $Sr_\theta \approx 0.024$  for initially turbulent axisymmetric and thin mixing layers of jets at relatively low Reynolds numbers less than 100,000.

Now, the frequency of the first peak observed in the LES noise spectrum is at  $Sr_D \approx 4.15$ . This is equal to one half of the shear layer instability frequency. Thus, the shear layer instability frequency corresponds to  $Sr_D \approx 8.3$ . We can easily convert this Strouhal frequency based on nozzle exit diameter to a Strouhal frequency based on the initial momentum thickness. Our shear layer's initial momentum thickness is  $\delta_\theta/D_j \approx 3 \times 10^{-3}$ . Thus the instability frequency of our shear layer is  $Sr_\theta = 8.3 \times 0.003 = 0.0249$ . This value is close to the instability frequency observed in initially turbulent shear layers. It is also known that the instability frequency of the shear layer is somewhat sensitive to the shape of the initial velocity profile. To re-iterate, the initial state of the shear layer has an effect on the instability frequency as well.

As discussed earlier, the turbulence intensity variation along the nozzle lip line of our shear layer looks quite similar to that of an initially laminar shear layer. Thus, we believe that the transitional state of the nozzle exit boundary layer makes our shear layer act more or less like an initially laminar shear layer and this causes additional noise generation due to vortex pairing, which is known to take place in jets with initially laminar shear layers. Also, note here that even though we have a jet with initially transitional shear layers, our jet's  $Re_\theta$  is about the same as the lower limit of the  $Re_\theta$  range for the laminar jets which were found to have vortex pairing noise by Bridges and Hussain [13]. Jets with initially turbulent shear layers typically have significantly larger values of  $Re_\theta$ . It is possible that the low  $Re_\theta$  in our case plays a role in vortex pairing as well, but this is just a speculation at this point and needs to be investigated further.

The experimental jet spectrum obviously does not display any peaks due to vortex pairing. The estimated boundary layer thickness of the experimental jet is about 7–8% of the nozzle diameter. Due to the design of the conic nozzle in the experiment [53], the experimental boundary layer at the nozzle exit becomes much thicker than that of the LES. Moreover, the experimental Reynolds number is five times that of the LES. The combination of the higher Reynolds number and much thicker boundary layer means a large  $Re_\theta$  and thus fully turbulent initial shear layers. This, in turn, guarantees no additional noise generation due to vortex pairing.

To estimate what the LES spectrum would look like if vortex pairing noise were completely absent, we can simply filter out the broadband peaks from our spectrum. The filtering process is done manually rather than by a band rejection filter. Given the present circumstances, this is the best we can do in order to have a somewhat meaningful comparison with the experiment. The black solid line in the spectra comparison figure is a curve fit to such a “filtered” spectrum. As can be seen from the figure, the shape of the “filtered” spectrum agrees with the experiment reasonably well. Some differences between the experimental and “filtered” spectra are not surprising, given the different nozzle exit conditions and Reynolds numbers. Also, the fact that the our “filtered” spectrum does not decay any faster than the experiment in the high frequency region can be used as evidence for sufficient grid resolution used in the numerical computation.



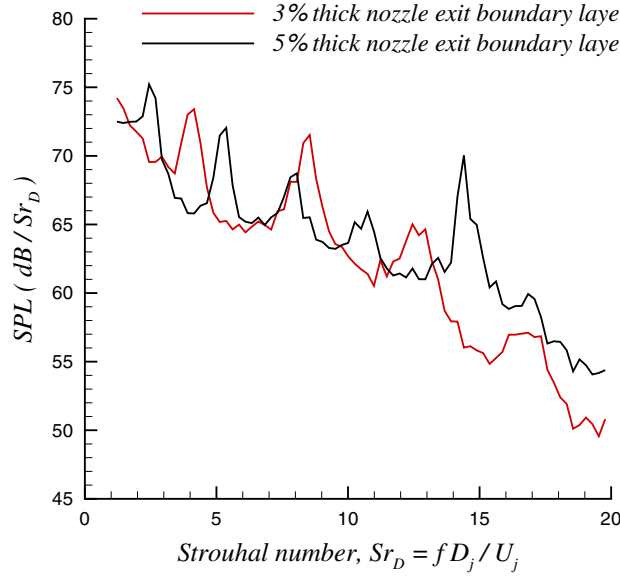


**Fig. 24** Comparison of the far field sideline noise spectra of the jets with different nozzle exit boundary layer thicknesses

In order to demonstrate the effect of the boundary layer thickness on the vortex pairing frequency and its harmonics, we performed a new simulation in which the boundary layer thickness at the nozzle inlet was doubled while all other test case parameters were kept the same as before. The new simulation has been run shorter than the previous one, but long enough to extract the far field sideline noise. In the new simulation, the boundary layer thickness at the nozzle exit reaches a value of  $\delta_{\text{exit}}/D_j \approx 5 \times 10^{-2}$  with a corresponding momentum thickness of  $\delta_\theta/D_j \approx 4.9 \times 10^{-3}$ . The far field sideline noise spectrum of the jet with the thicker boundary layer is compared with that of the jet with the thinner boundary layer in Fig. 24. As can be seen from the figure, the spectrum of the jet with the thicker boundary layer has its first peak at the new vortex pairing frequency of  $f_p = Sr_D \approx 2.45$ . The harmonics of this fundamental frequency are also present in the new spectrum. The shear layer instability frequency corresponding to this new vortex pairing frequency is  $Sr_D = 2 \times 2.45 = 4.9$ . This is the frequency based on the nozzle diameter. We can easily convert this to the frequency based on the initial momentum thickness as  $Sr_\theta = Sr_D \times \delta_\theta/D_j = 4.9 \times 0.0049 \approx 0.024$ , which is very close to the value obtained for the previous case. Interestingly, the very high frequencies in the thicker boundary layer spectrum seem to be more energetic compared to those in the thinner boundary layer case. Moreover, there does not seem to be a peak at the fourth harmonic ( $Sr_D \approx 12.25 - 12.5$ ), yet an energetic peak exists at the fifth harmonic. Nevertheless, the two LES spectra demonstrate that when the nozzle exit boundary layers are transitional, the initial shear layer instability frequency and thus the vortex pairing frequency (based on nozzle diameter) and its harmonics are directly dependent on the boundary layer thickness at the nozzle exit.

#### 4.2.6 Power spectral density of streamwise velocity fluctuations at vortex pairing frequency and its harmonics

In order to reveal the region where the vortex pairing noise and its harmonics are coming from, we have computed the spectra of the streamwise velocity fluctuations at all points within the mixing layer. This was done only for the jet with the thinner nozzle exit boundary layer. Velocity spectra were previously shown in the near-nozzle region to support the presence of vortex pairing. It is well understood that it is the turbulent velocity fluctuations that are somehow responsible for noise generation. Thus, examination of the spatial distribution of the spectral energy of the streamwise velocity fluctuations at the vortex pairing frequency and its harmonics can be useful for determining the source region of vortex pairing noise. The streamwise velocity fluctuation spectra were averaged along the azimuthal direction to get the final averaged power spectral density at each frequency on a two-dimensional  $xr$  plane. Figure 25 shows the power spectral density of the streamwise velocity fluctuations at the vortex pairing frequency,  $f_p = Sr_D \approx 4.15$ , while Fig. 26 depicts the power spectral density of the first harmonic of the vortex pairing frequency. As can be seen from the figure, the first harmonic

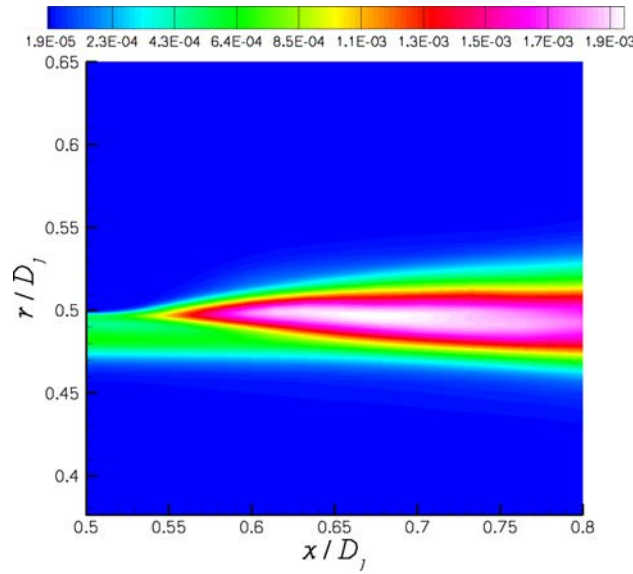


**Fig. 25** Power spectral density of streamwise velocity fluctuations at vortex pairing frequency,  $f_p$  on the  $xr$  plane. The edge of the nozzle lip is at  $x/D_j = 0.5$  and  $r/D_j = 0.5$ . The jet nozzle exit boundary layer thickness is  $\delta_{\text{exit}}/D_j \approx 3 \times 10^{-2}$

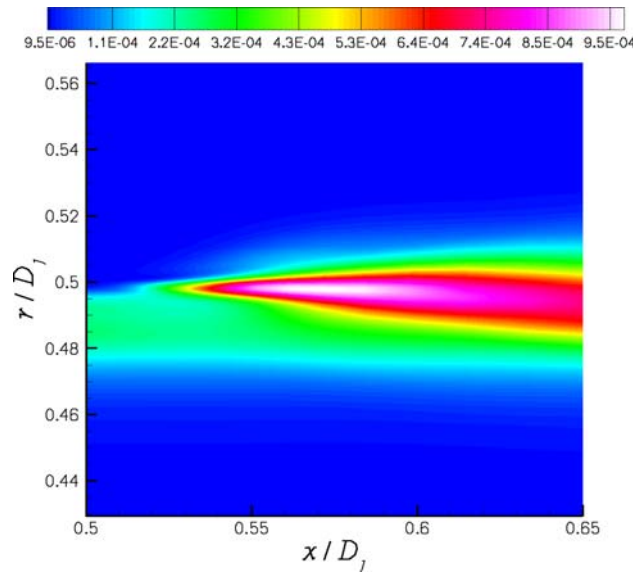


**Fig. 26** Power spectral density of streamwise velocity fluctuations at  $2f_p$  on the  $xr$  plane. The edge of the nozzle lip is at  $x/D_j = 0.5$  and  $r/D_j = 0.5$ . The jet nozzle exit boundary layer thickness is  $\delta_{\text{exit}}/D_j \approx 3 \times 10^{-2}$

at  $2f_p$ , which is also the vortex roll-up frequency of the shear layer, reaches its peak immediately downstream of the nozzle exit. This location is approximately the same as the peak location of the streamwise turbulence intensity in the shear layer which is shown in Fig. 27.

The power spectral density of the next three harmonics, that is at frequencies of  $3f_p$ ,  $4f_p$  and  $5f_p$ , depicted in Fig. 28, 29, and 30, have their peak regions very close to that of the first harmonic. On the other hand, the power spectral density at vortex pairing frequency reaches its peak further downstream at around  $x/D_j \approx 0.68$ , which is not that far from the nozzle exit, and slightly below the nozzle lip line where  $r/D_j = 0.5$ . The streamwise velocity fluctuations at the vortex pairing frequency and its first harmonic (vortex roll-up frequency) are the most energetic, while the remaining harmonics have progressively less spectral energy. It is evident from these figures that the spectral energy of the streamwise velocity fluctuations at the vortex pairing frequency and its harmonics reach their peaks in the initial region of the free shear layer very close to the nozzle exit.

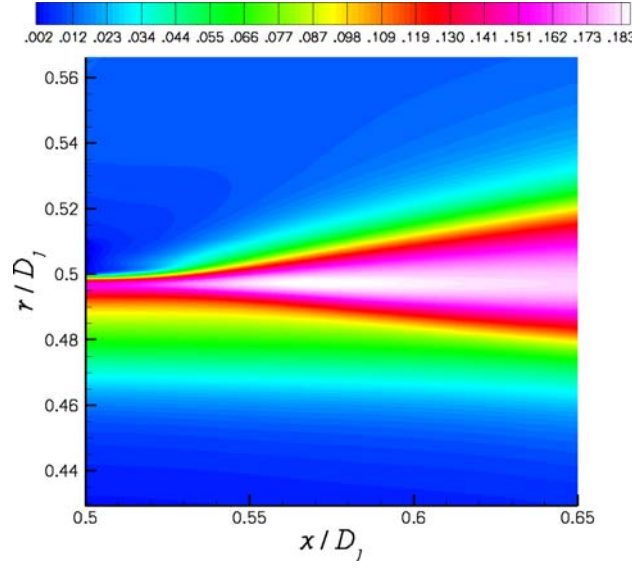


**Fig. 27** Contours of non-dimensional streamwise turbulence intensity on the  $xr$  plane. The edge of the nozzle lip is at  $x/D_j = 0.5$  and  $r/D_j = 0.5$ . The jet nozzle exit boundary layer thickness is  $\delta_{\text{exit}}/D_j \approx 3 \times 10^{-2}$

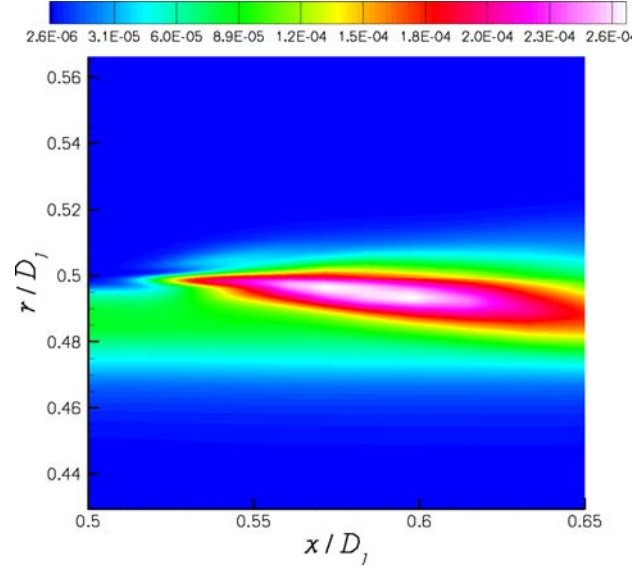


**Fig. 28** Power spectral density of streamwise velocity fluctuations at  $3f_p$  on the  $xr$  plane. The edge of the nozzle lip is at  $x/D_j = 0.5$  and  $r/D_j = 0.5$ . The jet nozzle exit boundary layer thickness is  $\delta_{\text{exit}}/D_j \approx 3 \times 10^{-2}$

This implies that the spectral peaks observed in the far field sideline noise spectrum at these frequencies are due to the noise generation in this region very near the nozzle exit. A snapshot of the instantaneous vorticity in the jet shear layers and the radiated noise previously shown in Fig. 9 provided additional evidence for the presence of a noise source in this region.

## 5 Conclusions

A unique computation that focuses solely on the high frequency noise generation in the near-nozzle region of a jet has been performed. When adjusted from model scale to jet engine scale, the high frequencies translate into the frequencies that are most annoying to the human ear. Accurate prediction of the very high frequency jet noise is therefore important for this reason. The highest resolved frequency in the present study is about

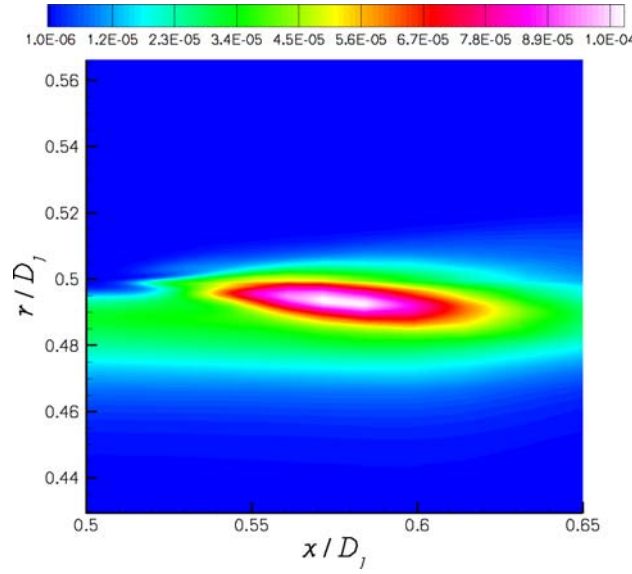


**Fig. 29** Power spectral density of streamwise velocity fluctuations at  $4f_p$  on the  $xr$  plane. The edge of the nozzle lip is at  $x/D_j = 0.5$  and  $r/D_j = 0.5$ . The jet nozzle exit boundary layer thickness is  $\delta_{\text{exit}}/D_j \approx 3 \times 10^{-2}$

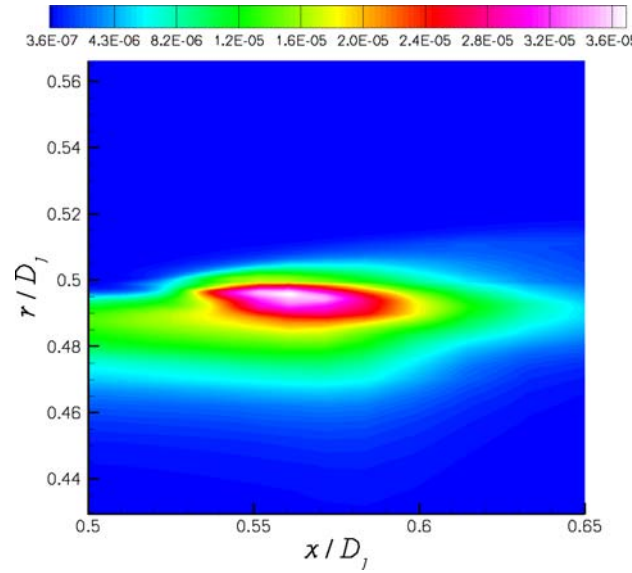


**Fig. 30** Power spectral density of streamwise velocity fluctuations at  $5f_p$  on the  $xr$  plane. The edge of the nozzle lip is at  $x/D_j = 0.5$  and  $r/D_j = 0.5$ . The jet nozzle exit boundary layer thickness is  $\delta_{\text{exit}}/D_j \approx 3 \times 10^{-2}$

an order of magnitude larger than that in most previous LES. Although we have attempted to generate fully turbulent boundary layers inside the nozzle, it appears that the nozzle exit boundary layer is in a transitional state, thus resulting in additional noise generation due to vortex pairing. The lack of a fully turbulent boundary layer at the nozzle exit is believed to be most likely due to imperfections in the inflow generation method used in this work. The effect of the nozzle exit boundary layer thickness on the vortex pairing Strouhal frequency (based on nozzle diameter) and its harmonics was demonstrated in a second simulation with a thicker nozzle exit boundary layer. On the other hand, previous research shows that jets with fully turbulent initial shear layers do not have such broadband peaks due to vortex pairing in the noise spectra. Thus, it is desirable to completely eliminate this surplus noise source in the computations to enable a more meaningful comparison with available experimental data of jets with initially turbulent shear layers. For this purpose, a longer nozzle section may be considered in future calculations. A longer nozzle section would certainly allow the boundary layers inside

the nozzle to age some more before reaching the nozzle exit. This, in turn, would make the state of the nozzle exit boundary layer more similar to a fully turbulent boundary layer. We expect that in such a scenario, the additional vortex pairing noise should disappear. However, this needs to be demonstrated in a new simulation that includes a longer nozzle section. This is one interesting topic for future research. Another possibility might be to further improve the rescaling–recycling procedure so that it allows fully turbulent boundary layer development within a shorter nozzle section. In these type of calculations, it would also be desirable to extend the computational domain farther downstream to capture the low frequency noise generation in that region. This, of course, requires additional grid points and computing resources.

The main objective of this work is to study the high frequency noise generated in the near-nozzle region by including the actual nozzle geometry. Admittedly, the lack of a fully turbulent boundary layer at our nozzle exit, which is most likely due to imperfections in the inflow generation method, and the possibly problematic features of the inflow generation method (discussed earlier) imply a considerable uncertainty regarding our nozzle flow. This uncertainty, in turn, makes it difficult to interpret the numerical results and make meaningful comparisons with experimental data. Nevertheless, we hope the lessons learned in this study will help guide future research activities towards resolving the limitations and deficiencies identified in this work.

A flow solver utilizing state-of-the-art numerical methods was used in the calculations. Multi-block and overset capabilities of the code allow grid density control in various regions of the computational domain while the high-order accurate schemes ensure a high-quality numerical solution. Implicit time stepping brings great savings in computing cost. These features of the code also allow the extension of the present methodology to simulations in more complex configurations, such as nozzles with tabs and chevrons that are under investigation for noise reduction. We expect that future developments in computing technology will enable the application of the present methodology to higher Reynolds number jet flows of technological interest using a lot more grid points.

**Acknowledgments** This research was funded by the Florida State University. This work was also partially supported by the National Center for Supercomputing Applications (NCSA) under the grant CTS050003 and utilized the NCSA Xeon Linux Cluster. The computations were also performed on the Cray XT3 system at the Pittsburgh Supercomputing Center. We thank K. Viswanathan for providing some of his experimental measurements to us.

## References

1. <http://www.ncsa.uiuc.edu/UserInfo/Resources/Hardware/XeonCluster>
2. <http://www.psc.edu/machines/cray/xt3/>
3. Andersson, N., Eriksson, L.E., Davidson, L.: Investigation of an isothermal Mach 0.75 jet and its radiated sound using large-eddy simulation and Kirchhoff surface integration. *Int. J. Heat Fluid Flow* **26**, 393–410 (2005)
4. Andersson, N., Eriksson, L.E., Davidson, L.: Large-eddy simulation of subsonic turbulent jets and their radiated sound. *AIAA J.* **43**(9), 1899–1912 (2005)
5. Andersson, N., Eriksson, L.E., Davidson, L.: LES prediction of flow and acoustic field of a coaxial jet. *AIAA Paper* 2005-2884 (2005)
6. Ashcroft, G., Zhang, X.: Optimized prefactored compact schemes. *J. Comput. Phys.* **190**(2), 459–457 (2003)
7. Barré, S., Bogey, C., Bailly, C.: Computation of the noise radiated by jets with laminar/turbulent nozzle-exit conditions. *AIAA Paper* 2006-2443 (2006)
8. Beam, R.M., Warming, R.F.: An implicit factored scheme for the compressible Navier–Stokes equations. *AIAA J.* **16**(4), 393–402 (1978)
9. Benek, J.A., Steger, J.L., Dougherty, F.C., Buning, P.G.: Chimera: A grid-embedding technique. Arnold Engineering Development Center Report AEDC-TR-85-64, Arnold Air Force Station, TN, USA (1986)
10. Biancherin, A., Lupoglazoff, N., Rahier, G., Vuillot, F.: Comprehensive 3d unsteady simulations of subsonic and supersonic hot jet flow-fields: Part 2: Acoustic analysis. *AIAA Paper* 2002-2600 (2002)
11. Birch, S.F.: A review of axisymmetric jet flow data for noise applications. *AIAA Paper* 2006-2602 (2006)
12. Bodony, D.J., Lele, S.K.: Review of the current status of jet noise predictions using large eddy simulation (invited). *AIAA Paper* 2006-0468 (2006)
13. Bridges, J.E., Hussain, A.K.M.F.: Roles of initial condition and vortex pairing in jet noise. *J. Sound Vibrat.* **117**(2), 289–311 (1987)
14. Choi, H., Moin, P.: Effects of the computational time step on numerical solutions of turbulent flow. *J. Comput. Phys.* **113**(1), 1–4 (1994)
15. Constantinescu, G.S., Lele, S.K.: A highly accurate technique for the treatment of flow equations at the polar axis in cylindrical coordinates using series expansions. *J. Comput. Phys.* **183**, 165–186 (2002)
16. DeBonis, J.R.: A large-eddy simulation of a high Reynolds number Mach 0.9 jet. *AIAA Paper* 2004-3025 (2004)
17. DeBonis, J.R., Scott, J.N.: Large-eddy simulation of a turbulent compressible round jet. *AIAA J.* **40**(7), 1346–1354 (2002)
18. Dong, T.Z.: On boundary conditions for acoustic computations in non-uniform mean flows. *J. Comput. Acoust.* **5**(3), 297–315 (1997)



19. Drubka, R.E.: Instabilities in the near field of turbulent jets and their dependence on initial conditions and Reynolds number. PhD Thesis, Illinois Institute of Technology, Chicago (1981)
20. Ekaterinaris, J.A.: Implicit, high-resolution, compact schemes for gas dynamics and aeroacoustics. *J. Comput. Phys.* **156**(2), 272–299 (1999)
21. Freund, J.B., Lele, S.K., Moin, P.: Calculation of the radiated sound field using an open Kirchhoff surface. *AIAA J.* **34**(5), 909–916 (1996)
22. Gaitonde, D.V., Visbal, M.R.: Padé-type higher-order boundary filters for the Navier–Stokes equations. *AIAA J.* **38**(11), 2103–2112 (2000)
23. Henshaw, W.: Ogen: An overlapping grid generator for overtone. <http://www.llnl.gov/casc/Overture>
24. Hussain, A.K.M.F., Zaman, K.B.M.Q.: An experimental study of organized motions in the turbulent plane mixing layer. *J. Fluid Mech.* **159**, 85–104 (1985)
25. Kim, J.W., Lee, D.J.: Generalized characteristic boundary conditions for computational aeroacoustics. *AIAA J.* **38**(11), 2040–2049 (2000)
26. Kim, J.W., Lee, D.J.: Generalized characteristic boundary conditions for computational aeroacoustics, part 2. *AIAA J.* **42**(1), 47–55 (2004)
27. Lele, S.K.: Compact finite difference schemes with spectral-like resolution. *J. Comput. Phys.* **103**(1), 16–42 (1992)
28. Lund, T.S., Wu, X., Squires, K.D.: Generation of turbulent inflow data for spatially-developing boundary layer simulations. *J. Comput. Phys.* **140**(2), 233–258 (1998)
29. Lupoglazoff, N., Biancherin, A., Vuillot, F., Rahier, G.: Comprehensive 3d unsteady simulations of subsonic and supersonic hot jet flow-fields: Part 1: Aerodynamic analysis. *AIAA Paper 2002–2599* (2002)
30. Lyrantzis, A.S.: Surface integral methods in computational aeroacoustics—from the (cf) near-field to the (acoustic) far-field. *Int. J. Aeroacoust.* **2**(2), 95–128 (2003)
31. Mohseni, K., Colonius, T.J.: Numerical treatment of polar coordinate singularities. *J. Comput. Phys.* **157**(2), 787–795 (2000)
32. Narayanan, S., Barber, T.J., Polak, D.R.: High subsonic jet experiments: Turbulence and noise generation studies. *AIAA J.* **40**(3), 430–437 (2002)
33. Paliath, U., Morris, P.J.: Prediction of noise from jets with different nozzle geometries. *AIAA Paper 2004-3026* (2004)
34. Paliath, U., Morris, P.J.: Prediction of jet noise from circular beveled nozzles. *AIAA Paper 2005-3096* (2005)
35. Piomelli, U., Balaras, E.: Wall-layer models for large-eddy simulations. *Ann. Rev. Fluid Mech.* **34**, 349–374 (2002)
36. Pulliam, T.H.: Artificial dissipation models for the Euler equations. *AIAA J.* **24**(12), 1931–1940 (1986)
37. Rai, M.M., Moin, P.: Direct numerical simulation of transition and turbulence in a spatially evolving boundary layer. *J. Comput. Phys.* **109**(2), 169–192 (1993)
38. Rizzetta, D.P., Visbal, M.R., Blaisdell, G.A.: A time-implicit high-order compact differencing and filtering scheme for large-eddy simulation. *Int. J. Numer. Methods Fluids* **42**(6), 665–693 (2003)
39. Sagaut, P., Garnier, E., Tromeur, E., Larchevêque, L., Labourasse, E.: Turbulent inflow conditions for large-eddy simulation of compressible wall-bounded flows. *AIAA J.* **42**(3), 469–477 (2004)
40. Schlichting, H.: Boundary-layer theory, 6th edn, chap. 14, pp 689–690. McGraw-Hill Book Company, New York (1968)
41. Sherer, S.E., Scott, J.N.: High-order compact finite-difference methods on general overset grids. *J. Comput. Phys.* **210**(2), 459–496 (2005)
42. Spalart, P.R.: Direct simulation of a turbulent boundary layer up to  $Re_\theta = 1410$ . *J. Fluid Mech.* **187**, 61–98 (1988)
43. Spalding, D.B.: A single formula for the law of the wall. *J. Appl. Mech.* **28**, 455–457 (1961)
44. Townsend, A.A.: The structure of turbulent shear flow. Cambridge University Press, Great Britain (1976)
45. Uzun, A.: 3-d large eddy simulation for jet aeroacoustics. PhD Thesis, School of Aeronautics and Astronautics, Purdue University, West Lafayette (2003)
46. Uzun, A., Blaisdell, G.A., Lyrantzis, A.S.: Application of compact schemes to large eddy simulation of turbulent jets. *J. Sci. Comput.* **21**(3), 283–319 (2004)
47. Uzun, A., Hussaini, M.Y., Streett, C.L.: Large-eddy simulation of a wing tip vortex on overset grids. *AIAA J.* **44**(6), 1229–1242 (2006)
48. Uzun, A., Lyrantzis, A.S., Blaisdell, G.A.: Coupling of integral acoustics methods with LES for jet noise prediction. *Int. J. Aeroacoust.* **3**(4), 297–346 (2004)
49. Visbal, M.R., Gaitonde, D.V.: Very high-order spatially implicit schemes for computational acoustics on curvilinear meshes. *J. Comput. Acoust.* **9**(4), 1259–1286 (2001)
50. Visbal, M.R., Morgan, P.E., Rizzetta, D.P.: An implicit LES approach based on high-order compact differencing and filtering schemes (invited). *AIAA Paper 2003-4098* (2003)
51. Visbal, M.R., Rizzetta, D.P.: Large-eddy simulation on curvilinear grids using compact differencing and filtering schemes. *J. Fluids Eng.* **124**(4), 836–847 (2002)
52. Viswanathan, K.: Aeroacoustics of hot jets. *J. Fluid Mech.* **516**, 39–82 (2004)
53. Viswanathan, K., Clark, L.T.: Effect of nozzle internal contour on jet aeroacoustics. *Int. J. Aeroacoust.* **3**(2), 103–135 (2004)
54. Viswanathan, K., Shur, M.L., Spalart, P.R., Strelets, M.K.: Computation of the flow and noise of round and beveled nozzles. *AIAA Paper 2006–2445* (2006)
55. Wu, X., Tristante, I.H., Page, G.J., McGuirk, J.J.: Influence of nozzle modelling in LES of turbulent free jets. *AIAA Paper 2005-2883* (2005)
56. Zaman, K.B.M.Q.: Effect of initial condition on subsonic jet noise. *AIAA J.* **23**(9), 1370–1373 (1984)